

---

*This copy is for your personal, non-commercial use only.*

---

**If you wish to distribute this article to others**, you can order high-quality copies for your colleagues, clients, or customers by [clicking here](#).

**Permission to republish or repurpose articles or portions of articles** can be obtained by following the guidelines [here](#).

**The following resources related to this article are available online at [www.sciencemag.org](http://www.sciencemag.org) (this information is current as of March 28, 2011):**

**Updated information and services**, including high-resolution figures, can be found in the online version of this article at:

<http://www.sciencemag.org/content/328/5985/1543.full.html>

**Supporting Online Material** can be found at:

<http://www.sciencemag.org/content/suppl/2010/06/16/328.5985.1543.DC1.html>

This article **cites 30 articles**, 4 of which can be accessed free:

<http://www.sciencemag.org/content/328/5985/1543.full.html#ref-list-1>

This article has been **cited by** 3 articles hosted by HighWire Press; see:

<http://www.sciencemag.org/content/328/5985/1543.full.html#related-urls>

This article appears in the following **subject collections**:

Chemistry

<http://www.sciencemag.org/cgi/collection/chemistry>

Microgravity enables us to venture into the regime of unprecedented long time evolution of the BEC up to 1 s (Fig. 4, B and D) with our setup. Our measurements reveal the above-mentioned suppression of the expansion in the  $x$  direction. Although our theory (black solid curves) predicts a linear growth, we observe a saturation. In addition, the observed widths in the  $z$  direction are larger than expected.

The origin of both deviations can be traced back to the fact that, during the expansion phase, the atoms are in the  $F = 2$ ,  $m_F = 2$  hyperfine state. Because of the long expansion times, these deviations represent a sensitive probe of tiny magnetic field gradients and curvatures. By including magnetic field curvatures on the order of a few microtesla per square millimeter in our simulation (black dotted curves), we are able to provide a qualitative explanation of the observed half widths. A coherent transfer of the BEC into the magnetically insensitive hyperfine state  $F = 2$ ,  $m_F = 0$  would avoid the influence of parasitic effects, and the implementation of this transfer is currently under way.

We anticipate a multitude of new research directions for ultracold, dilute quantum gases in free fall. A spin-off from our experiment is the possibility of preparing an extremely dilute wave packet at the lowest energy scales. This limit is difficult to reach in standard BEC ex-

periments but is relevant for the observation of quantum reflection (25) or Anderson localization (26, 27). Future atom interferometers in space will probe the boundary between GR and QM.

#### References and Notes

- C. W. Misner, K. S. Thorne, J. A. Wheeler, *Gravitation* (Freeman, San Francisco, 1973).
- E. A. Cornell, C. E. Wieman, *Rev. Mod. Phys.* **74**, 875 (2002).
- W. Ketterle, *Rev. Mod. Phys.* **74**, 1131 (2002).
- G. Stern *et al.*, *Eur. Phys. J. D* **53**, 353 (2009).
- E. Arimondo, W. Ertmer, W. P. Schleich, E. M. Rasel, Eds., *Proceedings of the International School of Physics "Enrico Fermi" Course CLXVIII "Atom Optics and Space Physics"* (IOS Press, Bologna, Italy, 2009).
- P. R. Berman, Ed., *Atom Interferometry* (Academic Press, San Diego, CA, 1997).
- A. Peters, K. Y. Chung, S. Chu, *Nature* **400**, 849 (1999).
- W. P. Schleich, M. O. Scully, in *New Trends in Atomic Physics, Proceedings of the Les Houches Summer School 1982, Session XXXVIII*, G. Grynberg, R. Stora, Eds. (North-Holland, Amsterdam, 1984), pp. 995–1124.
- I. Ciufolini, E. C. Pavlis, *Nature* **431**, 958 (2004).
- I. Ciufolini, *Nature* **449**, 41 (2007).
- I. Ciufolini, J. A. Wheeler, *Gravitation and Inertia* (Princeton Univ. Press, Princeton, NJ, 1995).
- S. Fray, C. Alvarez Diez, T. W. Hänsch, M. Weitz, *Phys. Rev. Lett.* **93**, 240404 (2004).
- S. Dimopoulos, P. W. Graham, J. M. Hogan, M. A. Kasevich, *Phys. Rev. Lett.* **98**, 111102 (2007).
- S. Dimopoulos, P. W. Graham, J. M. Hogan, M. A. Kasevich, S. Rajendran, *Phys. Rev. D Part. Fields Gravit. Cosmol.* **78**, 122002 (2008).
- A. E. Leanhardt *et al.*, *Science* **301**, 1513 (2003).
- A. Vogel *et al.*, *Appl. Phys. B* **84**, 663 (2006).
- W. Hänsel, P. Hommelhoff, T. W. Hänsch, J. Reichel, *Nature* **413**, 498 (2001).
- R. Folman, P. Krüger, J. Schmiedmayer, J. Denschlag, C. Henkel, *Adv. At. Mol. Opt. Phys.* **48**, 263 (2002).
- J. Fortágh, C. Zimmermann, *Rev. Mod. Phys.* **79**, 235 (2007).
- Y. Kagan, E. L. Surkov, G. V. Shlyapnikov, *Phys. Rev. A* **54**, R1753 (1996).
- Y. Castin, R. Dum, *Phys. Rev. Lett.* **77**, 5315 (1996).
- P. Storey, M. Olshanii, *Phys. Rev. A* **62**, 033604 (2000).
- Materials and methods are available as supporting material on Science Online.
- G. Nandi, R. Walser, E. Kajari, W. P. Schleich, *Phys. Rev. A* **76**, 063617 (2007).
- T. A. Pasquini *et al.*, *Phys. Rev. Lett.* **97**, 093201 (2006).
- J. Billy *et al.*, *Nature* **453**, 891 (2008).
- G. Roati *et al.*, *Nature* **453**, 895 (2008).
- This project is supported by the German Space Agency Deutsches Zentrum für Luft- und Raumfahrt (DLR) with funds provided by the Federal Ministry of Economics and Technology (BMWi) under grant number DLR 50 WM 0346. We thank the German Research Foundation for funding the Cluster of Excellence QUEST Centre for Quantum Engineering and Space-Time Research.

#### Supporting Online Material

www.sciencemag.org/cgi/content/full/328/5985/1540/DC1

Materials and Methods

References

5 March 2010; accepted 10 May 2010

10.1126/science.1189164

## Hot-Electron Transfer from Semiconductor Nanocrystals

William A. Tisdale,<sup>1</sup> Kenrick J. Williams,<sup>2,3\*</sup> Brooke A. Timp,<sup>2</sup> David J. Norris,<sup>1†</sup> Eray S. Aydil,<sup>1†</sup> X.-Y. Zhu<sup>2,3\*†</sup>

In typical semiconductor solar cells, photons with energies above the semiconductor bandgap generate hot charge carriers that quickly cool before all of their energy can be captured, a process that limits device efficiency. Although fabricating the semiconductor in a nanocrystalline morphology can slow this cooling, the transfer of hot carriers to electron and hole acceptors has not yet been thoroughly demonstrated. We used time-resolved optical second harmonic generation to observe hot-electron transfer from colloidal lead selenide (PbSe) nanocrystals to a titanium dioxide (TiO<sub>2</sub>) electron acceptor. With appropriate chemical treatment of the nanocrystal surface, this transfer occurred much faster than expected. Moreover, the electric field resulting from sub-50-femtosecond charge separation across the PbSe-TiO<sub>2</sub> interface excited coherent vibrations of the TiO<sub>2</sub> surface atoms, whose motions could be followed in real time.

The maximum theoretical efficiency of a standard silicon solar cell in use today is limited to ~31%, in part by the loss of any photon energy that exceeds the semiconductor bandgap ( $I$ ). Absorption of high-energy photons creates hot electrons and holes that cool quickly (within ~1 ps) to the band edges by sequential emission of phonons. There the carriers remain for hundreds of picoseconds or longer before slower processes such as radiative or nonradiative recombination occur. The goal of standard

solar cells is to extract these band-edge electrons and holes to produce electrical current. However, because of the initial cooling process, a substantial amount of solar energy has already been irreversibly lost. If instead, all of the energy of the hot carriers could be captured, solar-to-electric power conversion efficiencies could be increased, theoretically to as high as 66% (2). We can envision the realization of such a hot carrier solar cell in a semiconductor device where scattering among photoexcited electrons and reabsorp-

tion of additional photons in the conduction band is faster than hot-electron cooling, resulting in a quasi-equilibrium characterized by an electron temperature much higher than the lattice temperature. This is coupled with equally fast hot-electron transfer to an electron conductor in a narrow energy window (to minimize additional energy loss in the latter). The same argument applies to the holes.

A potential route to the above hot carrier solar cell is to use semiconductor nanocrystals, or quantum dots (3). In these materials, the quasi-continuous conduction and valence energy bands of the bulk semiconductor become discretized owing to confinement of the charge carriers. Consequently, the energy spacing between the electronic levels can be much larger than the highest phonon frequency of the lattice, creating a “phonon bottleneck” in which hot-carrier relaxation is only possible via slower multiphonon emission (4). For example, hot-electron lifetimes as long as ~1 ns have been

<sup>1</sup>Department of Chemical Engineering and Materials Science, University of Minnesota, Minneapolis, MN 55455, USA. <sup>2</sup>Department of Chemistry, University of Minnesota, Minneapolis, MN 55455, USA. <sup>3</sup>Department of Chemistry and Biochemistry, University of Texas, Austin, TX 78712, USA.

\*Present address: Department of Chemistry and Biochemistry, University of Texas, Austin, TX 78712, USA.

†To whom correspondence should be addressed: zhu@cm.utexas.edu (X.-Y.Z.), dnorris@umn.edu (D.J.N.), aydil@umn.edu (E.S.A.)

observed in quantum dots grown by molecular beam epitaxy (5). Even in colloidal quantum dots, which are coated with surfactant molecules that provide additional high-frequency vibrations for carrier relaxation, long lifetimes have been demonstrated through careful design of core-shell structures and control of interfaces (6). Such slowing of electron relaxation in core-shell quantum dots has recently been shown to allow the tunneling of hot electrons through the shells to surface trap states (7). Because of their ability to slow electronic relaxation, quantum dots can in principle enable extraction of hot carriers (to electron or hole conductors) before they cool to the band edges, leading to more efficient solar cells (8). However, hot-carrier transfer from nanocrystals to an electron or hole conductor has not yet been observed. Here, we show that electron transfer from the higher excited states of a colloidal semiconductor nanocrystal (PbSe) to a common electron acceptor (TiO<sub>2</sub>) is indeed possible and, with appropriate chemical treatment of the nanocrystal surface, occurs on an ultrafast time scale (<50 fs).

Although heterogeneous electron transfer from molecular chromophores to metal-oxide semiconductors has been probed with femtosecond time-resolved absorption (9), extending this approach to quantum dots has proved challenging. Differentiating between transient spectroscopic signatures of the photoexcited quantum dot, the reduced TiO<sub>2</sub> substrate, and the trap states is difficult (10). Further, to generate adequate signal, porous samples with large surface area but poorly defined interfaces are used. Consequently, reported time scales have spanned from picoseconds to microseconds (10–13).

Optical second harmonic generation (SHG) (14) is a much better technique for studying quantum-dot-to-semiconductor electron transfer because it offers femtosecond time resolution with sufficient sensitivity for well-defined crystalline interfaces. In a centrosymmetric semiconductor such as rutile TiO<sub>2</sub>, the second harmonic response originates only from the first few atomic layers near the surface (15). Thus, SHG should be extremely sensitive to changes in the local electronic environment resulting from interfacial electron transfer. Indeed, SHG has been used to probe ultrafast electron transfer at liquid-liquid interfaces (16). We show here that it can also be applied to semiconductor interfaces.

For fast electron transfer to occur, the nanocrystals should exhibit strong electronic coupling to the substrate. We chose colloidal PbSe quantum dots, as they are easy to prepare (17) and are better suited for electron transfer than other possible materials. In particular, PbSe has an extremely large exciton Bohr radius (46 nm) such that charge carriers in sub-10-nm diameter PbSe quantum dots are subject to strong quantum confinement effects (18), and their electronic wave functions will extend spatially well beyond the nanocrystal surface. This delocalization facilitates electron transfer if the nanocrystals

are close to an electron accepting substrate. We chose rutile TiO<sub>2</sub> for this role because it not only is technologically relevant and available as a single crystal but also has a very large density of accepting states. Further, the (110) surface of rutile TiO<sub>2</sub> is one of the most studied metal oxide interfaces, and the surface nonlinear susceptibility tensor and the origins of the second harmonic response are known (15).

Each sample consisted of one or two monolayers of PbSe nanocrystals deposited on atomically flat single-crystalline (110) TiO<sub>2</sub> (Fig. 1, A and B). The films were chemically treated with either hydrazine or 1,2-ethanedithiol (EDT) (19) to respectively remove or substitute for the oleic acid present on the nanocrystal surface. Both treatments enhance electronic coupling to the TiO<sub>2</sub> substrate and within the film (17, 20–22), but the bare surfaces produced by hydrazine result in stronger coupling (fig. S3). However, hydrazine can also leave many dangling bonds at the nanocrystal surface that can presumably act as scattering sites and accelerate electronic

cooling within the quantum dot. In contrast, thiols such as EDT passivate the nanocrystal surface and slow hot-electron relaxation in colloidal nanocrystals (6).

We tested PbSe nanocrystals ranging in diameter from 3.3 to 6.7 nm. As with all strongly confined semiconductor nanocrystals, the energy of excited electronic states in PbSe quantum dots increases with decreasing particle size. Thus, we first used ultraviolet photoelectron spectroscopy, in conjunction with optical absorption, to determine the energy of the lowest excited electronic state in our nanocrystals (19). We found that, regardless of particle size or chemical treatment, this state was always below the TiO<sub>2</sub> conduction band minimum (Fig. 1C). As a result, electron transfer from PbSe to TiO<sub>2</sub> should only be possible from hot electronic states of the quantum dot (12).

To study this electron transfer, we used 50-fs pulses of 810-nm (1.53-eV) light both to photoexcite (pump) the nanocrystals and detect (probe) the second harmonic response (19). The intensity of reflected second harmonic light at 405 nm ( $I^{2\omega}$ )

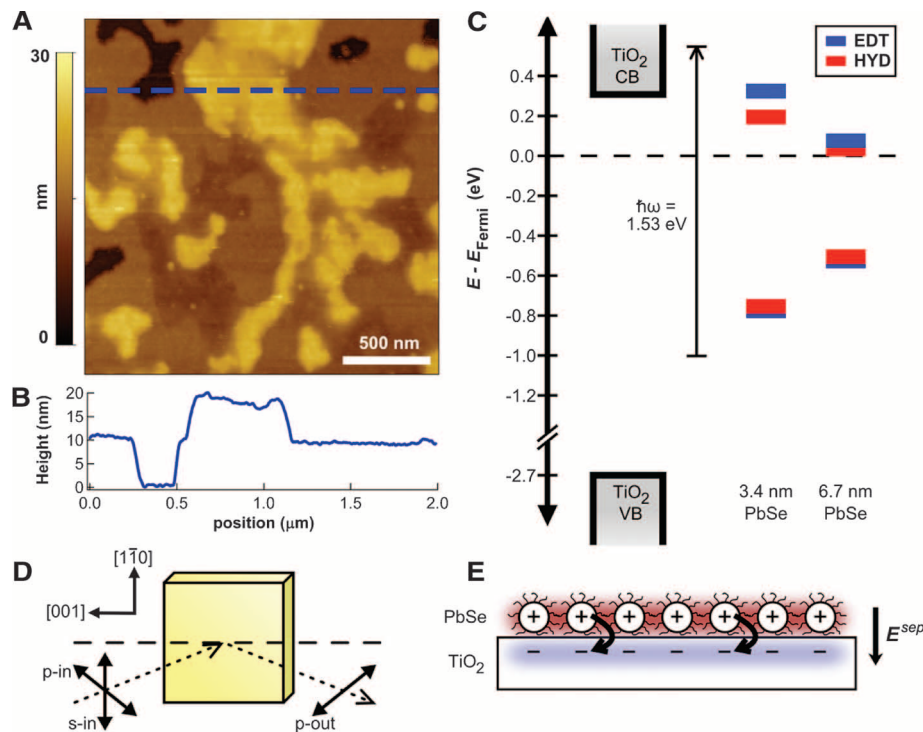


**Fig. 1.** (A) Atomic force micrograph showing the morphology of a ~1.5-monolayer film of 6.7-nm oleic acid-capped PbSe nanocrystals supported on atomically flat TiO<sub>2</sub>. (B) Line height profile corresponding to the dashed blue line in (A). The height of a monolayer (~11 nm) is the diameter of a nanocrystal (~7 nm) plus the thickness of the passivating organic layer (~2 nm) both above and below. (C) Alignment of highest occupied and lowest unoccupied quantum dot energy levels relative to the TiO<sub>2</sub> conduction band edge after chemical treatment of the nanocrystal surface. Alignment is determined by ultraviolet photoelectron and near-infrared absorption spectroscopies and indicates that electron transfer from the lowest excited state of the quantum dot is not energetically possible. The vertical arrow depicts symmetric photoexcitation of the PbSe quantum dots with 810-nm light. Numerical values are available in table S1. VB, valence band; CB, conduction band; EDT, 1,2-ethanedithiol; HYD, hydrazine. (D) Illustration of the crystal orientation and optical polarization used for SHG in reflection from the rutile (110) surface. (E) Schematic representation of the interfacial electric field generated by separation of electrons and holes across the PbSe-TiO<sub>2</sub> interface. Red indicates positive charge density; blue, negative charge density.

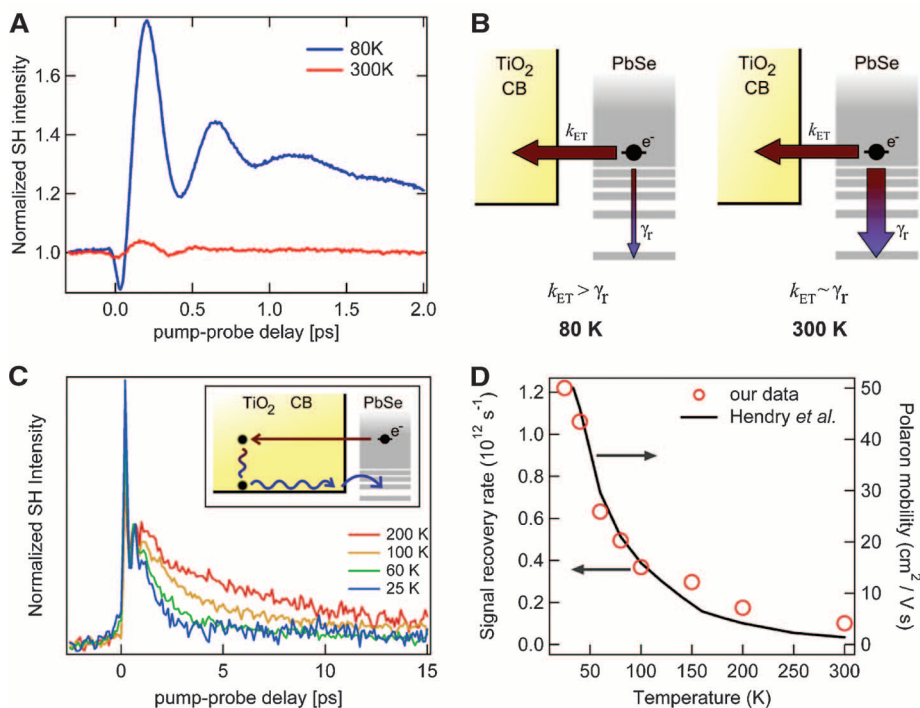


**Fig. 2.** (A) Time-resolved second harmonic response of the TiO<sub>2</sub> surface coated with 1.5 monolayers of hydrazine-treated 3.3-nm PbSe nanocrystals. The large rise in SHG intensity is indicative of efficient electron transfer from PbSe to TiO<sub>2</sub>. (B) Illustration of the competing pathways of interfacial electron transfer and intra-quantum-dot relaxation. At higher temperatures, hot-electron relaxation ( $\gamma_T$ ) becomes competitive with interfacial electron transfer ( $k_{ET}$ ). (C) Temperature-dependent decay of the pump-induced SHG signal enhancement; the absolute intensity has been normalized for pump-induced change to better illustrate the temperature-dependent recovery rate. (Inset) Cartoon showing ballistic electron injection (straight arrow) followed by phonon scattering and polaronic transport back to the interface (wavy lines) and then transfer back to the nanocrystal (curved arrow). (D) Correlation of SHG signal recovery rate (red circles) with the temperature-dependent polaron mobility perpendicular to the *c* axis in TiO<sub>2</sub> measured previously (29) assuming a temperature-independent polaron effective mass (black line).

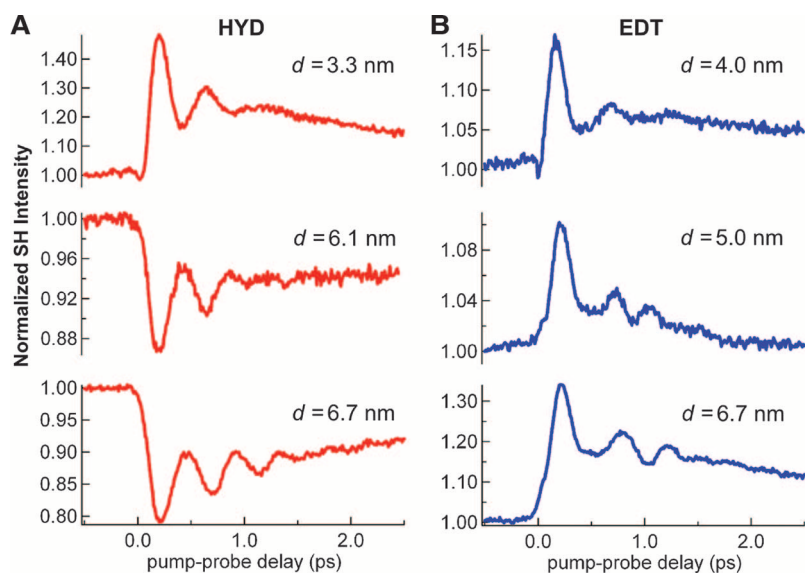


**Fig. 3.** Dependence of the time-resolved second harmonic response on nanocrystal size after treatment with (A) hydrazine (HYD) or (B) 1,2-ethanedithiol (EDT). The EDT-treated nanocrystals display efficient hot-electron transfer for all sizes studied, whereas substantial hot-electron transfer is only observed for smaller nanocrystals treated with hydrazine.

was recorded as a function of time delay between the pump and probe pulses. The polarization (p or s) of the fundamental was controlled and that of the second harmonic independently detected to isolate specific components of the nonlinear susceptibility tensor (Fig. 1D).

If electron transfer occurs, the separation of electrons and holes across the PbSe-TiO<sub>2</sub> interface generates an electric field,  $E^{sep}$ , oriented in the surface normal direction (Fig. 1E). SHG is highly sensitive to such slowly varying (relative to the optical frequency) electric fields because they can perturb the symmetry of the medium (23). This electric-field-induced second harmonic (EFISH) response has been used to study metal-electrolyte interfaces (24) and buried interfaces in field-effect transistors (25). When an interface already exhibits a large SHG signal,  $I^{2\omega}$ , even without an induced interfacial field [e.g., rutile (110) under the p-in/p-out configuration in Fig. 1D], the change in the SHG intensity,  $\Delta I^{2\omega}$ , due to electron transfer is proportional to  $E^{sep}$  as

$$\Delta I^{2\omega} = I^{2\omega} - I_0^{2\omega} \approx \eta (I^\omega)^2 E^{sep} \quad (1)$$

where  $I^{2\omega}$  is the intensity of the probe beam at the fundamental frequency  $\omega$ , and  $\eta$  contains the dependence on the dielectric function through linear and nonlinear Fresnel factors as well as the wavelength-, polarization angle-, and crystallographic orientation-dependent nonlinear susceptibility [see supporting online material (SOM) text 2] (26). If the charge-separated PbSe-TiO<sub>2</sub> interface is treated as a parallel-plate capacitor, then  $E^{sep}$  and the corresponding EFISH signal scale approximately linearly with the amount of separated charge. Consequently, electron transfer dynamics may be extracted directly from the time-resolved change in SHG intensity following photoexcitation of the PbSe film.

However, the analysis is complicated by the contribution to the SHG response from the quantum dots themselves. In particular, we expect photoexcitation of the quantum dots to lead to a decrease in SHG intensity, as is observed in molecular chromophores (16) and semiconductor nanowires (27). Indeed, we measure a drop in SHG intensity upon photoexcitation of our PbSe films supported on amorphous silica glass (at all quantum dot sizes, treatments, and temperatures). Because glass has a bandgap too wide to accept electron transfer from our quantum dots, we attribute this reduced intensity to their intrinsic SHG response (figs. S7 to S9).

In contrast to this drop, we observe a substantial rise in SHG intensity after photoexcitation of the quantum dots on TiO<sub>2</sub> at 80 K (Fig. 2A). This response is consistent with efficient hot-electron transfer from PbSe to TiO<sub>2</sub> for several reasons. First, the SHG signal rises on a time scale shorter than that of the laser pulse (50 fs). Such an ultrafast response would be expected for

the strong-coupling limit of electron transfer. Also, because the electronic relaxation time between the first two excited states in similar-sized PbSe quantum dots has been measured as 540 fs at 300 K (28), electron transfer must be appreciably faster than this to outpace the cooling process. Second, the magnitude of the ultrafast SHG response decreases with increasing temperature (Fig. 2A). As the PbSe quantum dots are warmed to 300 K, the time constant for electron transfer should be largely unaffected in the strong-coupling limit. However, the electronic relaxation rate is known to increase exponentially (28). Thus, at higher temperatures, cooling of hot electrons can compete with hot-electron transfer (Fig. 2B). Because cooled electrons cannot transfer to TiO<sub>2</sub> in our samples, accelerated cooling leads to a decrease in SHG signal. As a negative control, we

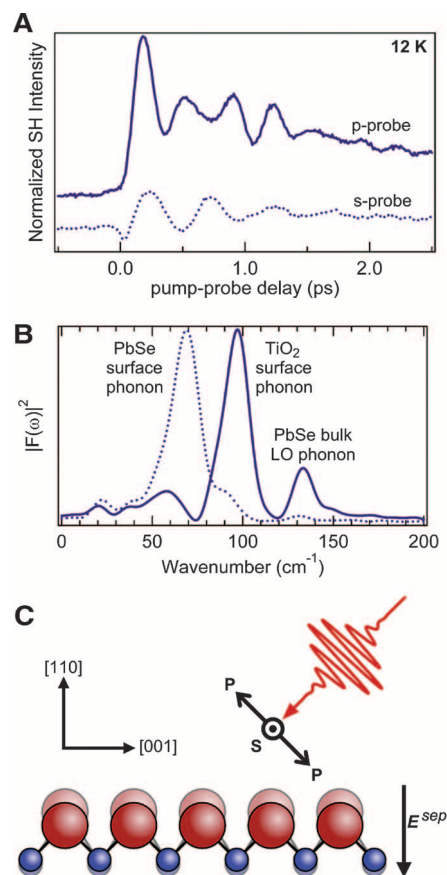


**Fig. 4.** Excitation of a coherent surface phonon by ultrafast electron transfer. **(A)** Time-resolved response at 12 K of the TiO<sub>2</sub> surface coated with 1.5 monolayers of EDT-treated 6.7-nm PbSe nanocrystals probed with either p- (solid) or s- (dotted) polarized light. **(B)** Fourier power spectrum of the oscillatory part of the SHG response curves shown in (A). With p-polarized light, a vibrational mode at  $97 \pm 5 \text{ cm}^{-1}$  attributed to a rutile (110) surface-specific coherent transverse optical phonon is observed. **(C)** Coherent vibration of the Ti-O zigzag bonds running along the [001] direction of the rutile (110) surface excited by ultrafast switching-on of the interfacial electric field resulting from sub-50 fs electron transfer.

observe no electron transfer when we decrease the pump photon energy to below the threshold necessary to reach the conduction band minimum of TiO<sub>2</sub> (fig. S10).

An analysis of the temperature-dependent decay of the pump-induced SHG signal on the picosecond time scale (Fig. 2C) is consistent with the temperature dependence of electron mobility in TiO<sub>2</sub>. If an electron transfers from PbSe to a resonant energy level within the TiO<sub>2</sub> conduction band, this electron would have considerable kinetic energy. It would move ballistically into TiO<sub>2</sub>, where electron-phonon scattering would bring it to the bottom of the conduction band, forming a polaron (29, 30). The electric field would eventually return the electron back to the TiO<sub>2</sub> surface for recombination with the positively charged nanocrystal and quenching of the EFISH signal (Fig. 2C, inset). An alternative interpretation is that the injected electron diffuses deep into bulk TiO<sub>2</sub> and is thus screened, resulting in the decay in SHG signal. In this scenario, recombination occurs on a much longer time scale (between consecutive probe pulses). We favor the former interpretation because computational study on the single-crystal TiO<sub>2</sub>(110) surface showed an order-of-magnitude faster time scale ( $\sim 100$  fs) for electron diffusion into the bulk TiO<sub>2</sub>, whereas back electron transfer from the near-surface region of TiO<sub>2</sub> to electron acceptors on the surface occurs on picosecond time scales, in agreement with the SHG decay time observed here (30). Regardless of which mechanism is operative, the rate of decay of the interfacial electric field would be proportional to the mobility of the polaron (see SOM text 4). Previous optical measurements determined this mobility in single-crystalline rutile TiO<sub>2</sub> as a function of temperature (29). The strong correlation between the decay rate of pump-induced SHG signal enhancement and the temperature-dependent polaron mobility (Fig. 2D) supports the conclusion that we are observing hot-electron transfer to delocalized TiO<sub>2</sub> conduction band states.

Further evidence is provided by the influence of nanocrystal size on the SHG response at 80 K. The pump-induced SHG response has two opposite contributions: the positive response from electron transfer to TiO<sub>2</sub> and the negative contribution from photoexcited nanocrystals. In hydrazine-treated samples (Fig. 3A), only smaller PbSe nanocrystals (3.3 nm) exhibit a signal characteristic of efficient electron transfer. The larger quantum dots (6.1 and 6.7 nm) exhibit a sharp drop in the SHG signal at zero pump-probe delay, indicative of a dominant contribution from photoexcited nanocrystals (figs. S8 and S9). The electronic state energies in the nanocrystals are size dependent, and these observations are related to which excited states are resonant with the TiO<sub>2</sub> conduction band. In larger nanocrystals, this resonance occurs for highly excited electronic states (above  $1P_e$ ) where ultrafast relaxation makes hot-electron transfer less competitive. In smaller nano-

crystals, the resonance occurs for the second excited state ( $1P_e$ ), and its relatively long lifetime makes hot-electron transfer to TiO<sub>2</sub> more efficient. Further, if the overall hot-electron relaxation rate could be slowed, electron transfer should compete effectively in all nanocrystal sizes. Indeed, for EDT-treated quantum dots, in which the overall electron relaxation is expected to be slower owing to effective surface passivation, we always observe the dominance of the positive SHG response from hot-electron transfer (Fig. 3B). The fluctuations in the magnitude of the pump-induced SHG signal intensity shown in Fig. 3 are representative of sample-to-sample variability in our data. We observe that these magnitude fluctuations arise primarily from batch-to-batch variations in the nanocrystals themselves and are presumably related to the structure and overall quality of the nanocrystal surface, which should play an important role in interfacial electron transfer.

One additional feature in our SHG data is the presence of large oscillations in the time-dependent response. For example, Fig. 2A shows a size-independent frequency of  $\sim 70 \text{ cm}^{-1}$  (2.1 THz or 8.7 meV). These oscillations have larger amplitude and slower dephasing at 80 K than at 300 K and are observed with both s- and p-polarized light. Though they are not present before removal of oleic acid from the nanocrystal surface, observation of these oscillations does not require interfacial electron transfer because they occur in hydrazine- and EDT-treated PbSe films supported on SiO<sub>2</sub> (figs. S8 and S9). On the basis of the frequency, its invariance with quantum dot size, and the independence of substrate material, yet sensitivity to surface chemical treatment, we attribute these oscillations to a coherent surface optical phonon mode in electronically coupled two-dimensional PbSe quantum dot assemblies. Close inspection of the EDT data (Fig. 3B) reveals frequency beating in the oscillations, which becomes more apparent at lower temperatures (Fig. 4A). A frequency-domain analysis of the p-polarized SHG waveform in Fig. 4A reveals three dominant Fourier components (Fig. 4B): the previously identified PbSe surface optical mode at  $\sim 70 \text{ cm}^{-1}$  (2.1 THz), the bulk PbSe longitudinal optical (LO) phonon at  $133 \pm 5 \text{ cm}^{-1}$  (4.0 THz) (31), and a mode at  $97 \pm 5 \text{ cm}^{-1}$  (2.9 THz) that dominates the p-polarized SHG signal but is much weaker for s-polarized probe light. The frequency of this last component is close to a predicted transverse optical phonon mode ( $104 \text{ cm}^{-1}$ ) of the rutile (110) surface of TiO<sub>2</sub>, which involves the motion of Ti and O atoms in and out of the surface plane (32). Under the p-in/p-out configuration with our crystal orientation (Fig. 1D), the SHG response of the (110) surface originates from anharmonic polarizability of the Ti-O zigzag bonds running along the [001] direction (Fig. 4C) (15). As these bonds stretch and compress in phase, we observe a time-dependent modulation of the SHG intensity resulting from accompanying fluctuations of the bond hyper-

polarizability. By symmetry, this modulation should arise if the driving electromagnetic wave contains an electric-field component along the Ti-O bond. Consequently, it is only observed with a p-polarized probe beam. For the s-polarized case, the SHG response arises mainly from the PbSe quantum dots, and the coherent phonon mode at  $70\text{ cm}^{-1}$  dominates.

We take the coherent surface phonon attributed to  $\text{TiO}_2$  as further evidence for hot-electron transfer. Such vibrations can be excited when electric fields near the surface are activated by optical pulses shorter than the vibrational period (33). Electron transfer across the PbSe- $\text{TiO}_2$  interface within the 50-fs width of the excitation pulse establishes an interfacial electric field faster than the characteristic response time of the surface atoms. These atoms subsequently find themselves in a vibrationally excited state of the new electric-field-induced minimum energy surface configuration. Time-domain fitting of an appropriate model function to the data in Fig. 4A (see fig. S11) reveals that the initial phase of this vibration is a cosine, consistent with a displacive excitation mechanism (see SOM text 3). The phase coherence of these collective motions is then lost over time because of elastic and inelastic scattering with bulk phonons.

These results indicate that hot-electron transfer from semiconductor nanocrystals to a technologically relevant electron acceptor is possible. This effect is expected to be of general relevance to other semiconductor nanocrystals and electron and hole conductors, provided the hot electrons and holes possess sufficiently long life-

times and the interfaces are properly controlled to enable ultrafast charge transfer. Moreover, if hot-electron (hole) transfer can be controlled to occur in very narrow energy windows to also minimize loss in the electron (hole) conductor, the highly efficient hot-carrier solar cell may be realized.

#### References and Notes

- W. Shockley, H. J. Queisser, *J. Appl. Phys.* **32**, 510 (1961).
- R. T. Ross, A. J. Nozik, *J. Appl. Phys.* **53**, 3813 (1982).
- A. P. Alivisatos, *Science* **271**, 933 (1996).
- A. J. Nozik, *Annu. Rev. Phys. Chem.* **52**, 193 (2001).
- K. Mukai, M. Sugawara, in *Self-Assembled InGaAs/GaAs Quantum Dots* (Academic Press, San Diego, CA, 1999), vol. 60, pp. 209–239.
- A. Pandey, P. Guyot-Sionnest, *Science* **322**, 929 (2008).
- A. Pandey, P. Guyot-Sionnest, *J. Phys. Chem. Lett.* **1**, 45 (2010).
- A. J. Nozik, *Physica E* **14**, 115 (2002).
- N. A. Anderson, T. Q. Lian, *Annu. Rev. Phys. Chem.* **56**, 491 (2005).
- J. L. Blackburn *et al.*, *J. Phys. Chem. B* **109**, 2625 (2005).
- I. Robel, V. Subramanian, M. Kuno, P. V. Kamat, *J. Am. Chem. Soc.* **128**, 2385 (2006).
- B. R. Hyun *et al.*, *ACS Nano* **2**, 2206 (2008).
- S. Y. Jin, T. Q. Lian, *Nano Lett.* **9**, 2448 (2009).
- Y. R. Shen, *Nature* **337**, 519 (1989).
- M. Omote *et al.*, *J. Phys. Cond. Mat.* **17**, S175 (2005).
- E. A. McArthur, K. B. Eisenthal, *J. Am. Chem. Soc.* **128**, 1068 (2006).
- D. V. Talapin, C. B. Murray, *Science* **310**, 86 (2005).
- F. W. Wise, *Acc. Chem. Res.* **33**, 773 (2000).
- See supporting material on Science Online.
- D. Yu, C. J. Wang, P. Guyot-Sionnest, *Science* **300**, 1277 (2003).
- J. M. Luther *et al.*, *ACS Nano* **2**, 271 (2008).
- K. J. Williams *et al.*, *ACS Nano* **3**, 1532 (2009).

- T. F. Heinz, in *Nonlinear Surface Electromagnetic Phenomena*, H. Ponnath, G. Stegeman, Eds. (Elsevier, Amsterdam, 1991), pp. 353–416.
- R. M. Corn, D. A. Higgins, *Chem. Rev.* **94**, 107 (1994).
- O. A. Aktsipetrov *et al.*, *Phys. Rev. B* **60**, 8924 (1999).
- A. Nahata, T. F. Heinz, *Opt. Lett.* **23**, 67 (1998).
- J. C. Johnson *et al.*, *Nano Lett.* **4**, 197 (2004).
- R. D. Schaller *et al.*, *Phys. Rev. Lett.* **95**, 196401 (2005).
- E. Hendry, F. Wang, J. Shan, T. F. Heinz, M. Bonn, *Phys. Rev. B* **69**, 081101 (2004).
- O. V. Prezhdo, W. R. Duncan, V. V. Prezhdo, *Prog. Surf. Sci.* **84**, 30 (2009).
- R. N. Hall, J. H. Racette, *J. Appl. Phys.* **32**, 2078 (1961).
- R. Lindsay *et al.*, *Phys. Rev. Lett.* **94**, 246102 (2005).
- Y. M. Chang, L. Xu, H. W. K. Tom, *Phys. Rev. Lett.* **78**, 4649 (1997).
- We thank K. S. Leschkes, A. Wolcott, C. Nelson, and G. Haugstad for assistance with PbSe nanocrystal synthesis and atomic force microscopy imaging. This work was supported by the U.S. Department of Energy (DE-FG02-07ER46468). Partial support from the NSF Nanoscale Interdisciplinary Research Team (NIRT) program (CBET-0506672) and the Materials Research Science and Engineering Center (MRSEC) programs (DMR-0819885) in the form of student assistantships to B.A.T. and W.A.T. are acknowledged. W.A.T. received support from a University of Minnesota Doctoral Dissertation Fellowship.

#### Supporting Online Material

www.sciencemag.org/cgi/content/full/328/5985/1543/DC1  
Materials and Methods

SOM Text

Figs. S1 to S11

Table S1

References

3 December 2009; accepted 4 May 2010

10.1126/science.1185509

# Crossover from Single-Step Tunneling to Multistep Hopping for Molecular Triplet Energy Transfer

Josh Vura-Weis,<sup>1</sup> Sameh H. Abdelwahed,<sup>2</sup> Ruchi Shukla,<sup>2</sup> Rajendra Rathore,<sup>2\*</sup> Mark A. Ratner,<sup>1\*</sup> Michael R. Wasielewski<sup>1\*</sup>

Triplet energy transfer (TT), a key process in molecular and organic electronics, generally occurs by either strongly distance-dependent single-step tunneling or weakly distance-dependent multistep hopping. We have synthesized a series of  $\pi$ -stacked molecules consisting of a benzophenone donor, one to three fluorene bridges, and a naphthalene acceptor, and studied the rate of TT from benzophenone to naphthalene across the fluorene bridge using femtosecond transient absorption spectroscopy. We show that the dominant TT mechanism switches from tunneling to wire-like hopping between bridge lengths 1 and 2. The crossover observed for TT can be determined by direct observation of the bridge-occupied state.

The rapid and efficient transport of energy and charge over tens to hundreds of nanometers in molecules underlies the performance of devices such as organic photovoltaics, thin-film transistors, and light-emitting diodes. Charge and energy transport is also crucial to many biological processes, such as long-

distance electron transfer in proteins (1) and the quenching of triplets in the bacterial photosynthetic reaction center by energy transfer cascades. (2) The study of charge transfer (CT) and triplet energy transfer (TT) in donor-bridge-acceptor (D-B-A) systems has demonstrated two general transport mechanisms—strongly distance-

dependent single-step tunneling and weakly distance-dependent multistep hopping, which is also known as wire-like transport (3). Optimizing TT efficiency is particularly important for improving organic and polymer light-emitting diode (OLED/PLED) performance, because injection of charge into the active layer of these devices generally leads to a 3:1 ratio of triplet to singlet excitons through spin statistics (4, 5), although the singlet exciton population may be higher in  $\pi$ -conjugated polymers (6). TT in PLEDs occurs both within and between chains (7), so that transport through noncovalent  $\pi$ -stacked molecules is important.

A major goal is to design molecules that exhibit multistep hopping in which charge or energy moves from a donor to the bridge and then later to the acceptor. Several CT studies have shown a crossover from tunneling to hopping as the bridge length increased, which

<sup>1</sup>Department of Chemistry and Argonne-Northwestern Solar Energy Research (ANSER) Center, Northwestern University, Evanston, IL 60208, USA. <sup>2</sup>Department of Chemistry, Marquette University, Post Office Box 1881, Milwaukee, WI 53201, USA.

\*To whom correspondence should be addressed: rajendra.rathore@marquette.edu (R.R.); ratner@chem.northwestern.edu (M.A.R.); m-wasielewski@northwestern.edu (M.R.W.)



## Supporting Online Material for

### **Hot-Electron Transfer from Semiconductor Nanocrystals**

William A. Tisdale, Kenrick J. Williams, Brooke A. Timp, David J. Norris,\*  
Eray S. Aydil,\* X.-Y. Zhu\*

\*To whom correspondence should be addressed: zhu@cm.utexas.edu (X.-Y.Z.),  
dnorris@umn.edu (D.J.N.), aydil@umn.edu (E.S.A.)

Published 18 June 2010, *Science* **328**, 1543 (2010)  
DOI: 10.1126/science.1185509

#### **This PDF file includes:**

Materials and Methods  
SOM Text  
Figs. S1 to S11  
Table S1  
References

## Supporting Online Material

### 1. Materials and methods

#### A. Preparation of PbSe thin films

##### *i. PbSe nanocrystal synthesis*

Colloidal PbSe nanocrystals were synthesized based on methods developed by Murphy *et al.* (S1) and Luther *et al.* (S2). In a typical synthesis, PbO (2.5 g), oleic acid (OA, 9 mL), and 1-octadecene (35 mL) were placed in a three-neck round-bottom flask. The reaction flask was then degassed to <40 mTorr while stirring vigorously and purged with dry nitrogen gas. The degassing process was repeated three times. The reaction vessel was heated to 180 °C under nitrogen and was maintained at that temperature for approximately 1 hr while the precursor solution turned optically clear. Meanwhile, a solution of Se dissolved in trioctylphosphine (TOPSe; 1.0 M, 21 mL total volume) was prepared and loaded into syringes inside a nitrogen glovebox. 15 mL of cold (0°C) anhydrous toluene was loaded into separate syringes. The TOPSe precursor was removed from the nitrogen glovebox and immediately injected into the reaction vessel. The temperature of the reaction solution was maintained at 150 °C during nanocrystal growth. UV/visible/near-infrared absorption measurements (Cary 5E) were used to monitor nanocrystal growth. Once the desired nanocrystal size was obtained (growth time varied from 30 s to 10 min), the heat source was removed from the reaction vessel and 15 mL of anhydrous toluene was swiftly injected into the vessel. The reaction vessel was rapidly cooled to room temperature using an ice bath. The reaction product was cannulated from the reaction vessel into a Schlenk flask and transferred into the nitrogen glovebox. All post-synthesis methods necessary to prepare clean nanocrystal dispersions were carried out in the nitrogen glovebox. The PbSe nanocrystals were precipitated out of the growth solution using a mixture of anhydrous methanol, butanol, and 200 proof ethanol (1:1:2, respectively) and isolated after centrifuging. The supernatant was discarded and the nanocrystals were re-dispersed in dry hexane. Precipitation with 200 proof ethanol followed by re-dispersion in dry hexane was repeated three times. The final product was

a solution (variable concentration) of oleic acid-capped PbSe nanocrystals (OA-PbSe) in hexane.

Nanocrystal size was determined by the energy of the first peak in the optical absorption spectrum as calibrated by Dai *et al.* (S3). The first exciton absorption energies for the OA-capped nanocrystals used in this study were 0.62 eV (2010 nm), 0.67 eV (1860 nm), 0.70 eV (1770 nm), 0.71 eV (1740 nm), 0.80 eV (1540 nm), 0.84 eV (1470 nm), 0.90 eV (1380 nm), 0.97 eV (1270 nm), 1.12 eV (1110 nm), and 1.14 eV (1080 nm) corresponding to nanocrystal diameters of 6.7 nm, 6.1 nm, 5.8 nm, 5.7 nm, 5.0 nm, 4.7 nm, 4.4 nm, 4.0 nm, 3.4 nm, and 3.3 nm, respectively. The same peak positions sized according to the work of Moreels *et al.* (S4) would yield nanocrystal diameters of 7.6 nm, 6.7 nm, 6.2 nm, 6.1 nm, 5.0 nm, 4.7 nm, 4.2 nm, 3.6 nm, 2.9 nm, and 2.8 nm, respectively.

ii. *TiO<sub>2</sub> substrate preparation*

Single crystal rutile TiO<sub>2</sub> was purchased from MTI Corporation (Richmond, CA). The <110> oriented crystals were 10 mm x 10 mm square, 1 mm thick, and mechanically polished on both sides. In-plane crystallographic orientation was determined by optical birefringence at 532 nm. Atomically flat surfaces were obtained by successive rinsing with 0.2 M NaOH then deionized water, followed by immersion in 1 M HCl under UV irradiation (254 nm) for 30 min and finally rinsing with deionized water and acetone in air (S5).

iii. *SiO<sub>2</sub> substrate preparation*

Laser quality fused silica flats were purchased from CVI Melles Griot (Albuquerque, NM). The 15 mm diameter x 1 mm thick circular substrates were cleaned by sonication in acetone followed by immersion in 1 M HCl then rinsing with deionized water in air.

iv. *Dip-coating*

All PbSe nanocrystal films were prepared in a controlled atmosphere argon glovebox to prevent PbSe oxidation. Clean substrates were rinsed with distilled hexane before partial

submersion in the OA-PbSe/hexane solution followed by withdrawal at a constant velocity of 1 cm/s. Desired coverage of the TiO<sub>2</sub> substrate was achieved by varying the concentration of the OA-PbSe/hexane solution (typically ~5 mg/mL) and verified by atomic force microscopy (AFM). The dip-coating process yielded samples that were optically uniform over a large area in the center of the substrate with drying lines visible at the top of the sample and along the edges.

v. *Hydrazine treatment*

Dried OA-PbSe films were submerged in a solution of 1 M hydrazine (HYD) in acetonitrile for 20 min at room temperature then dried under argon. The HYD concentration was chosen following the work of Law *et al.*, who showed removal of oleic acid without change in nanocrystal size or chemical reduction of PbSe (S6). The reaction time was chosen based on the continuous red shift of the first absorption peak during the first 10-15 min of HYD treatment followed by saturation of the red-shifted peak position with increasing duration of HYD treatment (S7).

HYD treatment results in nearly complete removal of the oleic acid surface ligands as verified by the disappearance of C-H stretch intensity at ~2920 cm<sup>-1</sup> in FTIR spectra (S7). Further, we find no evidence from either FTIR or XPS of nitrogen remaining in the film following HYD treatment (in agreement with Law *et al.* (S6)), suggesting that HYD has stripped the nanocrystal surface of OA but has not replaced it.

We have used AFM to look for morphological changes in monolayer PbSe films following HYD treatment (S7). As deposited, sub-monolayers of OA-capped PbSe will self-assemble into large single-layer islands of 2D hexagonal close-packed nanocrystals. After HYD treatment, the inter-nanocrystal spacing decreases and individual nanocrystals can no longer be spatially resolved, but optical absorption and height histogram analyses reveal that individual nanocrystals remain distinct (i.e., no ripening has taken place), in agreement with the findings of Law *et al.* (S6).

vi. *EDT treatment*

Following the work of Luther *et al.* (S2), dried OA-PbSe films were submerged in a solution of 0.1 M 1,2-ethanedithiol (EDT) in acetonitrile for 30 s at room temperature then dried under argon. XPS reveals the presence of sulfur within the EDT-treated PbSe film, supporting the conclusions of Luther *et al.* that EDT quantitatively replaces OA.

vii. *Mounting samples for laser measurements*

For laser experiments, each sample was clamped to a cold finger inside a Janis ST-300 liquid helium cryostat. To prevent exposure of the sample to ambient atmosphere, the cryostat was loaded and sealed inside the argon glovebox. The cryostat was evacuated to less than 1 mTorr base pressure for at least one hour using a liquid nitrogen-cooled cryopump before making measurements.

B. Sample characterization

i. *AFM*

Atomic force microscopy imaging (AFM) was carried out in a humidity-controlled ( $\leq 5\%$  RH) Agilent 5500 scanning probe microscope with a silicon tip ( $< 10$  nm radius of curvature) and rectangular cantilever (3 N/m nominal spring constant). Operation under low humidity and in AC mode with the oscillator in the net attractive regime was necessary to prevent transfer of nanocrystals to the silicon tip or otherwise disturb the PbSe film. See Ref. (S7) for further information.

ii. *XPS*

X-ray photoelectron spectroscopy (XPS) was used for compositional analysis of treated samples and to check for Pb oxidation following laser irradiation. Spectra were collected at room temperature in an ultrahigh vacuum spectrometer equipped with a hemispherical electron energy analyzer (Phi 5400). A Mg  $K_{\alpha}$  ( $h\nu = 1253.6$  eV) anode operated at 200 W was used as the X-ray source. The X-ray incident angle was  $5^{\circ}$  from surface normal and photoelectrons were collected at  $55^{\circ}$  from surface normal. A sealed transfer vessel was used for transporting samples from the glovebox to the XPS loading chamber air-free. Due to the high resistivity of the  $\text{TiO}_2$  substrates, some modest sample charging was

observed (less than 2 eV). To correct for this effect, energy scales were referenced to the Ti 2p binding energy of 458.6 eV (S8).

*iii. UPS*

Ultraviolet photoelectron spectroscopy (UPS) was used to determine interfacial alignment of occupied energy levels (see next section). All UPS spectra were collected at room temperature on the same instrument used for XPS. He-I radiation ( $h\nu = 21.2$  eV) was used as the UV light source, and the lamp power was set at 25 W. Incident light was  $50^\circ$  from the surface normal, and photoelectrons were collected along the sample surface normal direction with an analyzer pass energy of 4.45 eV and a sample bias of -8.0 V

*iv. FTIR and FT-NIR*

We use Fourier transform infrared (FTIR) and near-infrared (FT-NIR) spectroscopy in multiple total internal reflection geometry for spectroscopic characterization of PbSe nanocrystal films on TiO<sub>2</sub>. Large rutile single crystals oriented <110> and mechanically polished on both sides were purchased from Princeton Scientific Corporation (Princeton, NJ). These 1 mm thick crystals were cut to 32 mm x 10 mm with a polished  $45^\circ$  bevel on both ends to be used as ATR-FTIR waveguides. PbSe nanocrystal films were prepared on the exposed (110) surface as described. Measurements were carried out inside a nitrogen glovebox using a Nicolet 6700 FTIR-NIR spectrometer with either an InGaAs (FT-NIR) or liquid nitrogen-cooled mercury-cadmium-telluride (FTIR) detector. Periodic interference fringes in the absorption spectrum due to strong TiO<sub>2</sub> birefringence were removed by narrowband Fourier filtering.

C. Determining energy alignment using UPS and ATR-NIR

While published values of the electron affinity or work function of a material can be a useful starting point for estimating the band alignment between two different semiconductors, these estimates will never reflect the inevitable charge redistribution and interfacial dipole formation that occurs when two materials are brought into close electronic interaction. Consequently, meaningful conclusions about interfacial energy alignment can only be drawn from measurements made on the as-prepared composite

interface. To make these measurements, we use ultraviolet photoelectron spectroscopy (UPS), wherein the energies of near-surface occupied (valence) electronic energy levels are determined relative to the substrate Fermi level. Using UPS, the highest occupied electronic energy level of PbSe ( $1S_h$ ) can be placed relative to the  $\text{TiO}_2$  valence band edge and Fermi level as a function of nanocrystal size and surface chemical treatment. The position of the PbSe lowest unoccupied energy level ( $1S_e$ ) is inferred from optical absorption measurements made in attenuated total internal reflection geometry on identical PbSe monolayer films supported on  $\text{TiO}_2$  rutile (110) single crystal waveguides as described. Our measurements (summarized in Fig. 1C and Table S1) are in close agreement with the predictions of Hyun *et al.* (S9) who determined, based on corrected  $\mathbf{k}\cdot\mathbf{P}$  calculations and the cyclic voltammetry measurements of Jiang *et al.* (S10), that electron transfer from the lowest excited state of PbSe to  $\text{TiO}_2$  is energetically unfavorable for all PbSe nanocrystal sizes that can be reasonably prepared with available colloidal methods.

The photoemission spectrum of clean  $\text{TiO}_2$  (110) in the vicinity of the valence band maximum (VBM) is shown in Fig. S1 on both linear (panel A) and logarithmic (panel B) scales. Spectra are plotted on a binding energy (BE) scale, where  $\text{BE} = E - E_{\text{Fermi}}$ . As is standard for semiconductor VBM determination via UPS, the position of the VBM is obtained by extrapolation from the linear data or, more accurately, by the kink in the logarithmic representation marking the transition from occupied “true” valence band states to the continuum of defect-induced surface states extending to the Fermi level. We place the  $\text{TiO}_2$  VBM  $2.7 \pm 0.1$  eV below the Fermi level. Rutile  $\text{TiO}_2$  has an indirect band gap of 3.00-3.05 eV over a temperature range of 1.6 K to 300 K (S11), placing the  $\text{TiO}_2$  conduction band minimum (CBM) 0.3 eV above the Fermi level.

The near-surface valence band structure of clean  $\text{TiO}_2$  (110) is largely unchanged after treatment with either HYD or EDT (Fig. S2A). However, when the surface is covered with chemically treated PbSe nanocrystals (Fig. S2B), the  $\text{TiO}_2$  features are attenuated and we see an increase in photoemission intensity within the energetic region of the  $\text{TiO}_2$  band gap. These band gap features increase in intensity with increasing nanocrystal coverage, demonstrating that these features belong to PbSe occupied states. When the

surface is covered with untreated OA-capped PbSe nanocrystals, we see only the attenuated TiO<sub>2</sub> VB; the VB features of the nanocrystal are not visible because of the thick shell of insulating ligands surrounding the nanocrystals. Since the density of electronic states within a semiconductor nanocrystal does not follow the same  $E^{1/2}$  dependence of bulk semiconductors, extrapolation of the photoemission intensity is not appropriate for nanocrystal HOMO level determination. The HOMO level or VBM is determined by the inflection point in the log-scale representation of the data at the low-binding energy edge of nanocrystal valence emission intensity. This position is most accurately obtained from the second derivative of a smoothed spectrum, i.e. where  $d^2 \ln I/dE^2 = 0$ .

We use two different PbSe nanocrystal sizes for the UPS experiments:  $d = 3.4$  nm and  $d = 6.7$  nm. Absorption spectroscopy of these nanocrystals with OA shows the first exciton peaks at 1110 nm ( $d = 3.4$  nm) and 2010 nm ( $d = 6.7$  nm), corresponding to optical gaps of 1.12 eV and 0.62 eV, respectively. Removal of the OA ligands by HYD leads to a red shift of the first exciton peak by 0.15 eV and 0.07 eV for  $d = 3.4$  and 6.7 nm, respectively. Thus, the optical gap of nanocrystals within the treated films is  $E_G = 0.97$  eV for  $d = 3.4$  nm and  $E_G = 0.55$  eV for  $d = 6.7$  nm. With EDT treatment, the red-shift of the first exciton transition energy is much smaller, in the range of 0.02-0.04 eV across all sizes (Fig. S3), and below the energy resolution of the UPS measurement. We take the optical gaps of the EDT-treated 2D nanocrystal assemblies to be  $E_G = 1.1$  eV for  $d = 3.4$  nm and  $E_G = 0.6$  eV for  $d = 6.7$  nm. The optical gap is smaller than the transport gap by the exciton binding energy, which generally depends on particle size but is expected to be on the order of a few tens of meV for PbSe due to the large dielectric constant (S12). This exciton binding energy is negligible within our experimental energy resolution, so we take the optical gap as equal to the transport gap.

The size dependence of the nanocrystal VBM is summarized in Fig. S4. As the nanocrystal size is decreased from  $d = 6.7$  nm to  $d = 3.4$  nm, the VBM shifts further away from the Fermi level, from BE =  $0.55 \pm 0.1$  eV to 0.7-0.9 eV. To more accurately determine the energetic shift, we have normalized the intensities of the two spectra in the nanocrystal VB region and shifted the  $d = 3.4$  nm spectrum horizontally to match the

spectrum for  $d = 6.7$  nm. We find that a binding energy shift of  $-0.25 \pm 0.05$  eV provides a nearly perfect match, as shown in Fig. S4B. Given the optical gaps of 0.55 and 0.97 eV for the HYD-treated films of  $d = 6.7$  nm and 3.4 nm, respectively, the difference in the nanocrystal LUMO levels is  $0.17 \pm 0.05$  eV. Thus, with decreasing nanocrystal size, the HOMO and LUMO levels shift away from the Fermi level nearly symmetrically. We find that the two different chemical treatments give similar interfacial VB alignment for both 3.4 nm (Fig. S4C) and 6.7 nm nanocrystals (not shown). Our findings are summarized in Fig. 1C and Table S1.

#### D. Time-resolved optical second harmonic generation (TR-SHG)

##### *i. Laser system*

A home-built 78 MHz Ti:sapphire oscillator (830 nm, 30 fs, 50 nm bandwidth at FWHM, 200 mW) with peak-to-peak stability better than 0.01% seeds a regenerative amplifier operated at 250 kHz (Coherent RegA 9050). The output of the amplifier is compressed (810 nm, 50 fs, 30 nm bandwidth at FWHM,  $\pm 0.1\%$  peak-to-peak), attenuated, and then split into two equal intensity beams. One beam (the pump) passes through a variable-length delay line before recombining with the other beam (the probe) on the sample surface. The polarization state of each beam is independently controlled with quartz waveplates and long-wave pass filters are placed immediately in front of the cryostat (in which the sample is mounted) to remove any residual 405 nm light generated in the waveplates or other optical components. The uncoated 1.5 mm thick cryostat windows are made from Suprasil II, a high-quality amorphous silica glass transparent at 405 nm and exhibiting negligible second order nonlinear susceptibility at normal incidence. The pump and probe beams are softly focused non-collinearly at a mutual angle of  $\sim 3^\circ$  onto the sample surface. The projection of the beam on the sample at  $45^\circ$  incidence is a  $260 \mu\text{m} \times 360 \mu\text{m}$  ellipse, as measured by the knife-edge technique. The laser power is kept sufficiently low to maintain a spatially averaged fluence of less than  $1 \text{ mJ}/\text{cm}^2$  for both pump and probe pulses. The entire laser system is housed within a light-tight enclosure.

For the two-color measurements (variable wavelength pump, 810 nm probe, Fig. S10), a portion of the amplifier output is sent to a double-pass optical parametric amplifier

(Coherent OPA 9850) for conversion to longer wavelengths in the near- or mid-infrared. The remaining 810 nm light is used for the probe beam, as above.

By conservation of momentum, second harmonic (SH) light generated from the sample surface is collinear with each reflected beam. When pump and probe pulses are overlapped on the sample in space and time, a third nonlinear signal at the sum of the two frequencies (sum-frequency, SF) is generated at a wave vector in between the two reflected SH signals. This SF signal is equivalent to the cross-correlation of the pump and probe laser pulses and provides a convenient mechanism for optimizing spatial overlap, minimizing pulse width, and calibrating “time zero” at the sample surface.

For all samples at all temperatures, the time-resolved second harmonic (TR-SH) response is observed to be independent of pump beam polarization. Unless otherwise indicated, all TR-SH data shown in this report were collected with orthogonally polarized pump and probe beams to minimize coherent artifacts near  $t = 0$  (particularly scattered SF light).

*ii. Data acquisition*

For the laser power and focusing conditions used in this study, the reflected fundamental light is  $\sim 10^{10}$  times more intense than the SH light propagating collinearly with it. We use a combination of dichroic mirrors (Layertec), color glass filters (CVI Melles Griot), dispersion gratings (Oriel Cornerstone 130 monochromator), and a large-work function photomultiplier tube (Hamamatsu R4220P) to achieve the desired spectral filtering. A polarizing prism is used to select only the p-polarized component of the reflected SH light. The signal from the PMT is amplified and fed to a lock-in amplifier (Stanford Research SR850), which is phase-locked with a 500 Hz optical chopper placed in the probe beam path (to distinguish the SH light associated with the probe beam from ambient 405 nm light or scattered SH light associated with the pump). A desktop computer records data from the lock-in amplifier and controls the motorized linear delay stage (Newport – 0.1  $\mu\text{m}$  per step/0.67 fs time resolution).

Because of the excellent stability of the laser system ( $\pm 0.1\%$  peak-to-peak rms as measured on an oscilloscope), shot-to-shot normalization was not necessary. The primary

noise source in these measurements is Poisson noise arising from the natural sampling statistics of counting discrete photons. The signal-to-noise ratio (SNR) improves as  $\sqrt{N}$ , where  $N$  is the total number of photons collected. Consequently, a typical TR-SH waveform takes about one hour to collect and is the result of averaging  $\sim 20$  scans at 300 time points per scan. High-resolution data such as that presented in Figs. 2A & 4A represents the average of  $\sim 80$  scans collected over the course of five hours. We choose to collect and average many scans instead of dwelling at each time point for an extended period of time so that we can detect (and ensure that we have avoided) changes to the TR-SH waveform over the course of the experiment.

### iii. Control experiments

#### a) Power dependence and laser-induced damage to the nanocrystal film

Due to the quadratic dependence of the EFISH signal on incident probe laser power,  $\Delta I^{(2\omega)} \approx \eta (I^{(\omega)})^2 E^{sep}$ , it is desirable to use high laser fluences in order to obtain large SNRs. However, high laser power can damage the PbSe nanocrystals and the TR-SH response under high intensity light may not reflect the dynamics of electron transfer under the low excitation conditions characteristic of solar radiation. To assess the effects of prolonged laser irradiation, we continuously monitor the TR-SH waveform during data collection. For the chemically-treated PbSe films investigated here, the only variations in the TR-SH waveform we observe over the course of hours are small changes in the magnitude of the signal due to drifting laser power. However, we do observe qualitative changes in the TR-SH response after a few minutes of laser exposure for PbSe films thicker than  $\sim 3$  ML. This observation is further evidence that hot electron transfer to  $\text{TiO}_2$  is an efficient mechanism for energy dissipation within the photoexcited nanocrystal film.

A pump laser fluence of  $1 \text{ mJ/cm}^2$  corresponds to an average photoexcitation of one electron-hole pair per nanocrystal for the smallest PbSe nanocrystals used. We have investigated the power dependence of the SH response to laser fluences as low as  $0.03 \text{ mJ/cm}^2$ . Only the magnitude of the SH response changes; the dynamics and overall shape of the TR-SH response function are unchanged. We also routinely check the TR-SH

response at multiple locations on the sample surface. Again, the magnitude of the response varies due to spatial variation in PbSe surface concentration, but the dynamics are unchanged. Dynamics are also invariant with storage of the sample within the cryostat for days at a time or transferring the sample back to the glovebox for later re-evaluation.

The oxidation of PbSe nanocrystals in air is well documented (S2). When the PbSe surface becomes oxidized, peaks in the XPS spectrum due to core level photoemission from oxygen-bound Pb will appear 1.0 eV higher in binding energy than the selenium-bound Pb (S13). To be sure that laser irradiation does not lead to photo-oxidation of the PbSe surface under the residual atmosphere within the cryostat (base pressure < 1 mTorr), we measured the XPS spectrum of a 1 ML HYD-treated film after one day's worth of laser experiments (Fig. S5). The sample was transferred to a sealed vessel inside the glovebox for air-free transfer to the XPS vacuum chamber. The Pb 4f peaks are gaussian in shape without detectable asymmetry toward higher binding energies, indicating that the PbSe surface is free from oxidation.

#### b) System relaxation

The 250 kHz repetition rate of the laser system is ideal for femtosecond nonlinear optics at the surface of centrosymmetric media. The small second-order nonlinear susceptibility of these materials and the quadratic dependence of SH signal intensity on laser pulse fluence means that, at conservative laser intensities, only a few SH photons are collected per laser pulse. The high repetition rate of the 250 kHz system (as compared to the typical 1 kHz rate of a standard regenerative amplifier) means that adequate SNRs can be obtained over shorter lengths of data collection time. To be sure that the  $(250 \text{ kHz})^{-1} = 4 \text{ } \mu\text{s}$  period between laser pulses is sufficiently long for the system to relax to the ground state, we verify that at negative time-delays (probe arriving before pump) the SH intensity reflected from the sample surface is unchanged when the pump beam is blocked.

#### c) TR-SH response of the bare substrate surface

The TR-SH response of bare TiO<sub>2</sub> (110) and bare SiO<sub>2</sub> (amorphous fused silica) is shown in Fig. S6. The TR-SH waveform is featureless for both substrates at 300 K and 80 K as

well as after treatment with HYD or EDT. The Fermi level of our TiO<sub>2</sub> samples is 0.3 eV below the CBM, so electronic transitions from occupied defect states within the TiO<sub>2</sub> band gap to the conduction band should be possible with our 1.5 eV photon energy. However, the density of these defect states in our single crystal samples is too small to produce a detectable change in SH intensity within our signal-to-noise capabilities ( $\pm$  0.5% of the background level).

d) TR-SH response of OA-capped PbSe nanocrystals on TiO<sub>2</sub>

The TR-SH response of OA-capped PbSe nanocrystals on TiO<sub>2</sub> is shown in Fig. S7. Oleic acid (OA) is a carboxylic acid with an 18-carbon straight-chain aliphatic tail. The OA shell surrounding the nanocrystal electronically insulates the PbSe core from the TiO<sub>2</sub> substrate. Consequently, hot electron transfer from OA-capped PbSe nanocrystals to TiO<sub>2</sub> is not observed. The TR-SH response of OA-capped PbSe nanocrystal films is featureless (within our signal-to-noise capabilities) for all sizes, temperatures, and substrate materials investigated here.

e) TR-SH response of chemically treated PbSe nanocrystals on SiO<sub>2</sub>

The TR-SH response of HYD- and EDT-treated PbSe nanocrystals on SiO<sub>2</sub> is shown in Figs. S8 & S9 for nanocrystals 6.7 nm in diameter. PbSe coherent phonon oscillations identical to those observed for PbSe nanocrystals on TiO<sub>2</sub> are apparent. The SH intensity drops upon photoexcitation then recovers over the course of picoseconds. A similar decrease in SH intensity followed by ps signal recovery has been observed in ZnO nanowires (S14) and was explained by a difference in the hyperpolarizability of conduction and valence band electrons. The recovery of the SH signal from ZnO was thought to reflect the dynamics of hot electron relaxation. Our findings are consistent with this explanation of the recovery dynamics. We notice strong dependence of the recovery rate on temperature. At 300 K (Fig. S8A) the SH signal recovery time constant is  $\sim$ 0.5 ps, whereas at 80 K (Fig. S8B) the time constant is  $\sim$ 3 ps. These time constants follow the same temperature trend reported for  $1P_e$  to  $1S_e$  relaxation in PbSe nanocrystals (S15) and are approximately five times faster than those reported for similar sizes. It is important to emphasize that the SH signal recovery dynamics of PbSe nanocrystals on

SiO<sub>2</sub> (slower recovery at lower temperatures) show the *opposite* temperature trend from that observed for PbSe nanocrystals on TiO<sub>2</sub> (faster recovery at lower temperatures), supporting our assertion that these dynamics are of different origin.

The fact that OA-capped PbSe nanocrystals do not exhibit either coherent phonon oscillations or a drop in SH intensity upon photoexcitation (Fig. S7) is intriguing. We also notice that static SH intensities increase by an order of magnitude following treatment of OA-PbSe:SiO<sub>2</sub> samples with either HYD or EDT. While the change in second-order susceptibility may be due to strong inter-nanocrystal electronic coupling, it is also possible that increased SH intensities are due to charge trapping within the chemically treated film. PbSe crystallizes in the rock salt structure, which is centrosymmetric and bulk-SHG inactive. Local separation of charge within the PbSe nanocrystal film (i.e. by electron or hole trapping at the nanocrystal surface) may “activate” the PbSe core for SHG via electric field-induced symmetry-breaking, increasing static SH intensities and revealing dynamic processes that would otherwise be hidden from observation.

All TR-SHG data collected on nanocrystal-covered SiO<sub>2</sub> substrates exhibit a broad (500-800 fs FWHM) symmetric peak in intensity centered at  $t = 0$  that is due to efficient sum-frequency (SF) generation of light scattered from the nanocrystal film and internally reflected off the back surface of the SiO<sub>2</sub> substrate (S16, S17). The intensity of this scattered SF component increases substantially following treatment with HYD or EDT due to changes in the nanocrystal film morphology as observed via AFM (S7). This phenomenon is not observed on TiO<sub>2</sub> because 405 nm light generated on the back surface of the crystal is absorbed within the 1 mm thick TiO<sub>2</sub> substrate before reaching the front surface. The data shown in Figs. S8 & S9 have had this SF component removed for clarity.

f) Dependence of the TR-SH response on pump wavelength

As a negative control, we decreased the pump photon energy to below the threshold necessary to reach the conduction band minimum of TiO<sub>2</sub> (Fig. S10). The data show a clear rise in SHG intensity following photoexcitation with 810 nm (1.5 eV) light, whereas

no discernible change in intensity is observed when the sample is pumped at 1180 nm (1.0 eV). In order to make a fair comparison, it is necessary to maintain the same average excitation across all wavelengths. The average excitation,  $\eta$ , is the average number of photons absorbed (or electron-hole pairs created) per nanocrystal, and is calculated as  $\eta = J\sigma$ , where  $J$  is the number of photons per laser pulse per unit area and  $\sigma$  is the absorption cross section of a nanocrystal at the pump wavelength (S18). As  $\sigma$  varies with photon energy, the photon fluence  $J$  must be adjusted so that  $\eta$  is conserved. For the data shown in Fig. S10,  $J$  was chosen to maintain  $\eta = 1.0$  electron-hole pairs per nanocrystal per laser pulse.

## 2. The electric field-induced second harmonic response (EFISH)

The electric field-induced second harmonic (EFISH) response at the surface of a centrosymmetric material was first discovered by Lee, Chang, & Bloembergen in 1967 (S19). SHG, in general, is highly sensitive to slowly varying or dc electric fields because of the potential for such fields to perturb the symmetry of the medium. Phenomenologically, the EFISH response is treated as a four-wave mixing process modulated by an effective fourth-rank nonlinear susceptibility tensor  $\chi_{eff}^{(3)}(2\omega = \omega + \omega + 0)$  that contains contributions from both the surface and the bulk (S20, S21). The total second-order nonlinear (NL) polarization within a semiconductor is given by,

$$\begin{aligned} \mathbf{P}^{NL}(2\omega) &= \mathbf{P}^{BD}(2\omega) + \mathbf{P}^{BQ}(2\omega) + \mathbf{P}^S(2\omega) + \mathbf{P}^{EFISH}(2\omega) \\ &= \epsilon_o \left[ \begin{aligned} &\chi_{bulk}^{(2)}(2\omega) : \mathbf{E}(\omega)\mathbf{E}(\omega) + \chi_{bulk}^{(Q)} : \mathbf{E}(\omega)\nabla\mathbf{E}(\omega) + \dots \\ &\chi_{surf}^{(2)}(2\omega) : \mathbf{E}(\omega)\mathbf{E}(\omega) + \chi_{eff}^{(3)} : \mathbf{E}(\omega)\mathbf{E}(\omega)\mathbf{E}(0) \end{aligned} \right], \end{aligned} \quad (S1)$$

where the superscripts BD, BQ, and S refer to bulk dipole, bulk quadrupole, and surface dipole contributions, respectively. For centrosymmetric media such as rutile TiO<sub>2</sub>, the BD term vanishes due to inversion symmetry. In the absence of a dc electric field, the BQ and S contributions may be of comparable magnitude, but can be separated by careful control of geometry and polarization (S22). Such work has been done for the rutile (110) surface of TiO<sub>2</sub> and it was determined that the surface dipole contribution dominates the SH

response – particularly for the geometry used in our electron transfer studies (S23). In this case, the total nonlinear polarization reduces to surface dipole and EFISH contributions,

$$\mathbf{P}^{NL}(2\omega) = \mathbf{P}^S(2\omega) + \mathbf{P}^{EFISH}(2\omega).$$

The reflected SH field can be divided into the sum of background (surface dipole response when  $E^{(dc)} = 0$ ) and EFISH contributions (S24),

$$\begin{aligned} \mathbf{E}^{(2\omega)} &= \mathbf{E}_o^{(2\omega)} + \mathbf{E}_{EFISH}^{(2\omega)} \\ &\propto \chi_{surf}^{(2)} (E^{(dc)} = 0) : \mathbf{E}^{(\omega)} \mathbf{E}^{(\omega)} + \chi_{eff}^{(3)} : \mathbf{E}^{(\omega)} \mathbf{E}^{(\omega)} \mathbf{E}^{(dc)} \end{aligned} \quad (\text{S2})$$

For the purpose of clarity, we have neglected the linear and nonlinear Fresnel factors. The experimentally observed SHG intensity is,

$$\begin{aligned} I^{(2\omega)} &= \left| \mathbf{E}_0^{(2\omega)} + \mathbf{E}_{EFISH}^{(2\omega)} \right|^2 \\ &= \alpha \left| \chi_{surf}^{(2)} \right|^2 (I^{(\omega)})^2 + \beta (\chi_{surf}^{(2)*} \chi_{eff}^{(3)} + \chi_{surf}^{(2)} \chi_{eff}^{(3)*}) (I^{(\omega)})^2 E^{(dc)} + \gamma \left| \chi_{eff}^{(3)} \right|^2 (I^{(\omega)})^2 (E^{(dc)})^2, \end{aligned} \quad (\text{S3})$$

where  $\alpha$ ,  $\beta$ , and  $\gamma$  are constants that depend on geometry,  $\chi^*$  is the complex conjugate of  $\chi$ , and  $I^{(\omega)}$  is the incident laser field intensity. Because rutile TiO<sub>2</sub> (110) exhibits a large background SH signal in the absence of an external electric field under the geometry used here (i.e.  $\chi_{surf}^{(2)} \gg \chi_{eff}^{(3)}$ ), the third term in Eq. (S3) can be neglected. Under such conditions, the observed SH intensity is linear in the electric field strength,

$$\begin{aligned} I^{(2\omega)} &\approx I_0^{(2\omega)} + \Delta I^{(2\omega)} \\ &\approx I_0^{(2\omega)} + \eta (I^{(\omega)})^2 E^{(dc)}, \end{aligned} \quad (\text{S4})$$

with  $\eta$  containing nonlinear susceptibilities and geometric factors. If we take the charge-separated PbSe-TiO<sub>2</sub> interface to be a parallel plate capacitor, then the electric field strength at the interface due to charge separation is (see Section 4 below),

$$\begin{aligned} E^{(dc)} &\equiv E^{sep} = \frac{1}{\epsilon_r \epsilon_o} \frac{2Q^{sep}}{A}, \\ &\propto Q^{sep} \end{aligned} \quad (\text{S5})$$

where  $Q^{\text{sep}}$  is the amount of separated charge. As a result, we expect the EFISH signal to scale approximately linearly with  $Q^{\text{sep}}$ ,

$$\Delta I^{(2\omega)} \propto Q^{\text{sep}}. \quad (\text{S6})$$

### 3. Time-domain fitting of the TR-SH response function

It is evident from inspection of the TR-SH response in Figs. 2A & 4A that interfacial electron transfer occurs within the first 100 fs following photoexcitation of the PbSe nanocrystals. However, the presence of large-amplitude coherent phonon oscillations obscures the underlying dynamics of electron transfer. Additionally, insight into the mechanism of coherent phonon excitation can be acquired through knowledge of the initial phase of the oscillator (S25). To uncover these underlying electron transfer dynamics and elucidate the initial phase of each vibrational mode, we fit the entire time-resolved SHG waveform to a phenomenological model for the EFISH response based on first-order kinetics, taking into account the finite width of the laser pulse. While this simplistic model fails to account for quantum dynamic processes such as electronic dephasing that are important on these timescales, it nonetheless reproduces most of the features of the time-resolved SHG waveform and provides an estimate of the electron transfer time constant.

The total time-dependent SH signal,  $S(t)$ , can be expressed as the sum of the constant background SH intensity, the time-dependent EFISH intensity, and up to three sinusoidal coherent phonon contributions (as indicated by the Fourier transforms shown in Fig. 4B),

$$S(t) = S_0 + \Delta S_{EFISH}(t) + \Delta S_T(t) + \Delta S_p(t) + \Delta S_{LO}(t). \quad (\text{S7})$$

The last three terms in Eq. (S7) with subscripts T, p, and LO refer to the  $\text{TiO}_2$  surface phonon, the PbSe surface phonon, and the PbSe bulk LO phonon, respectively. The EFISH contribution is proportional to the total number of electrons,  $N_e(t)$ , that have transferred to  $\text{TiO}_2$ ,

$$\Delta S_{EFISH}(t) = \alpha N_e(t), \quad (\text{S8})$$

where  $\alpha$  is a proportionality constant.  $N_e(t)$  is found by solving a system of linear ordinary differential equations,

$$\begin{aligned} \frac{dN_{nc}^*}{dt} &= R \cdot I_{pump}(t) - \frac{N_{nc}^*}{\tau_{ET}}, \\ \frac{dN_e}{dt} &= \frac{N_{nc}^*}{\tau_{ET}} - \xi N_e \end{aligned}, \quad (S9)$$

where  $N_{nc}^*$  is the population of photoexcited nanocrystals,  $\tau_{ET}$  is the electron transfer time constant,  $\xi$  is the electron transport/recombination rate, and  $R$  is a constant that depends on the laser fluence and absorption cross-section of the nanocrystals.  $I_{pump}(t)$  is the gaussian pump pulse intensity envelope,

$$I_{pump}(t) = \exp\left(-\frac{(t-t_0)^2}{(width/\sqrt{2\ln 2})^2}\right), \quad (S10)$$

where  $width$  is the FWHM of the pump-probe cross correlation. The number of  $\text{TiO}_2$  surface phonons generated per unit time is proportional to the instantaneous rate of electron transfer,  $K_{ET}(t)$ , which is equal to,

$$K_{ET}(t) = \frac{N_{nc}^*}{\tau_{ET}}. \quad (S11)$$

The total time-dependent modulation of the SHG intensity by the  $\text{TiO}_2$  surface phonon population is found by convolving an exponentially decaying sine wave with  $K_{ET}(t)$ ,

$$\Delta S_T(t) = A_T \left[ K_{ET}(t) * \sin(\omega_T t + \varphi_T) \exp(-\Gamma_T t) \right], \quad (S12)$$

where the symbol  $*$  denotes a convolution.  $A_T$ ,  $\omega_T$ ,  $\varphi_T$ , and  $\Gamma_T$  are the phonon amplitude, frequency, phase, and dephasing rate, respectively. The time-dependent modulation of the SH intensity by the PbSe surface optical and bulk LO phonon modes is found similarly,

$$\begin{aligned} \Delta S_p(t) &= A_p \left[ I_{pump}(t) * \sin(\omega_p t + \varphi_p) \exp(-\Gamma_p t) \right] \\ \Delta S_{LO}(t) &= A_{LO} \left[ I_{pump}(t) * \sin(\omega_{LO} t + \varphi_{LO}) \exp(-\Gamma_{LO} t) \right] \end{aligned}, \quad (S13)$$

with each contribution convolved with the pump pulse intensity envelope because these modes are directly generated by the laser pulse.

To perform the fit, we employ a parallel genetic optimization algorithm. The best-fit curve to the data in Fig. 4A is shown in Fig. S11A. The non-oscillatory component of the TR-SH signal,  $S_{\text{non-osc}}(t) = SH_0 + \Delta S_{\text{EFISH}}(t)$ , is shown in Fig. S11B. We extract an electron transfer time constant of  $\tau_{\text{ET}} = 31 \pm 5$  fs (assigned uncertainty is the standard deviation of the fit parameter). The three sine components included in the fitting function have best-fit frequencies of  $\omega_p = 66.8 \text{ cm}^{-1}$ ,  $\omega_T = 95.3 \text{ cm}^{-1}$ , and  $\omega_{LO} = 131.0 \text{ cm}^{-1}$ ; phase  $\varphi_p = 3\pi/2 \text{ rad}$  (cosine-like/displacive),  $\varphi_T = 3\pi/2 \text{ rad}$  (cosine-like/displacive), and  $\varphi_{LO} = \pi \text{ rad}$  (sine-like/impulsive); and dephasing times  $\Gamma_p^{-1} = 520 \text{ fs}$ ,  $\Gamma_T^{-1} = 1100 \text{ fs}$ , and  $\Gamma_{LO}^{-1} = 950 \text{ fs}$ .

#### 4. The electric field strength and the temperature dependence of the SH signal recovery

Because the distance over which electrons and holes are separated (10-20 nm, see below) is much smaller than the diameter of the laser spot on the sample (hundreds of microns), the charge-separated interface can be modeled as an infinite parallel plate capacitor. The electric field at the interface (denoted in this section by the symbol  $\mathbf{E}$  to avoid confusion with the symbol for energy,  $E$ ) is given by,

$$\mathbf{E} = \frac{1}{\epsilon\epsilon_0} \frac{2Q^{sep}}{A}, \quad (S14)$$

where  $2Q^{sep}$  is the total amount of separated charge (each “plate” has charge  $Q^{sep}$ ),  $A$  is the irradiated area,  $\epsilon_r$  is the dielectric constant at the interface, and  $\epsilon_0$  is the permittivity of free space. The surface concentration of nanocrystals is determined by the packing of OA-capped nanocrystals within the monolayer as formed during the dip-coating process. High-resolution AFM imaging of individual nanocrystals within the film reveals a hexagonally close-packed 2D array (S7). For efficient electron transfer from a complete monolayer with 10 nm lattice constant,  $Q^{sep}/A = 1.9 \times 10^{-3} \text{ C}\cdot\text{m}^{-2}$ . The dielectric constant of rutile  $\text{TiO}_2$  perpendicular to the optical axis maintains its “low frequency” value of  $\epsilon_r = 86$  to frequencies as high as 0.3 THz (S24). The corresponding dielectric constant of PbSe is  $\epsilon_r = 210$  (S26). A composite value of  $\epsilon_r = 100$  corresponds to an electric field strength of  $3.8 \times 10^4 \text{ V cm}^{-1}$ . Thus, the electric field at the interface is comparable to the field strengths required for observation of large EFISH signals at Si-SiO<sub>2</sub> interfaces in field-effect transistors (S21).

After a fast rise in SH intensity due to ultrafast electron transfer, the EFISH signal decays over the course of picoseconds due to electron transport back to the  $\text{TiO}_2$  surface and subsequent back-electron transfer to the ionized nanocrystal. The overall process involves ballistic electron injection followed by hot electron relaxation to form band-edge polarons then Drude-like transport back to the surface under the action of the interfacial electric field. Hot electron relaxation in ionic semiconductors such as  $\text{TiO}_2$  is dominated by the emission of polar optical (LO) phonons (S28), which varies weakly over the

temperature range considered here due to the very high frequency of these modes in TiO<sub>2</sub> (200 cm<sup>-1</sup>/24 THz/100 meV) (S29). The ballistic mean free path,  $\lambda_b$ , of an electron travelling in rutile perpendicular to the optical axis and having excess energy  $E^{ex}$  is given by,

$$\begin{aligned}\lambda_b &= \langle \tau_b \rangle \cdot v_b \\ &= \langle \tau_b \rangle \cdot \left( \frac{2E^{ex}}{m_{\perp}^*} \right)^{1/2},\end{aligned}\quad (S15)$$

where  $\langle \tau_b \rangle$  is the mean scattering time,  $v_b$  is the velocity of the ballistic electron, and  $m_{\perp}^* = 1.2m_e$  is the electron band mass (S30). A discrete flux of electrons crossing the surface will establish an energetically relaxed band-edge electron (polaron) density distribution of the form  $n = n_0 \exp(-z/\lambda_b)$ , where  $n$  is the local number concentration of electrons (polarons) and  $z$  is the coordinate in the surface normal direction, with  $z=0$  at the surface and positive values of  $z$  increasing within the bulk of the crystal. The electron (polaron) population will drift back toward the interface under the action of the interfacial electric field where electron transfer back to the nanocrystal film reduces the total amount of separated charge, given by,

$$Q^{sep} = Ae \int_{z=0}^{z=\infty} n(z,t) dz . \quad (S16)$$

Upon integration, we find that the total amount of separated charge decreases over time according to,

$$Q^{sep} = Q_0 \exp\left(-\frac{v_p t}{\lambda_b}\right), \quad (S17)$$

where  $v_p = \mu \mathbf{E}$  is the polaron drift velocity and  $\mu$  is the polaron mobility. Since the change in SH intensity is proportional to the total amount of separated charge,  $\Delta I^{(2\omega)}(t) \propto Q^{sep}(t)$ , we may fit the SH signal to the form,

$$I^{(2\omega)}(t) = I_0^{2\omega} + \Delta I_0^{2\omega} \exp(-\xi t), \quad (S18)$$

with the pump-induced SH signal decay rate,  $\xi$ , given by the expression  $\xi = \mu\mathbf{E}/\lambda_0$ . Since  $\lambda_0$  varies only weakly with temperature, we may (to first approximation) conclude that the temperature dependence of the SH signal recovery rate is contained in the temperature dependence of the polaron mobility,

$$\xi(T) \propto \mu(T), \quad (\text{S19})$$

as demonstrated by the correlation shown in Fig. 2D.

A typical polar optical scattering time of  $\langle\tau_b\rangle = 50$  fs and hot electron excess energy of  $E_{ex} = 0.2$  eV lead to a ballistic mean free path of  $\lambda_b = 12$  nm. For an electric field strength of  $3 \times 10^4$  V cm<sup>-1</sup> and a polaron mobility at 80 K of  $20$  cm<sup>2</sup> V<sup>-1</sup> s<sup>-1</sup>, we arrive at an expected SH signal recovery time constant of  $\sim 2$  ps, or  $\xi = 0.5 \times 10^{12}$  s<sup>-1</sup>, which is close to the value at 80 K shown in Fig. 2D.

## 5. Supplementary Figures

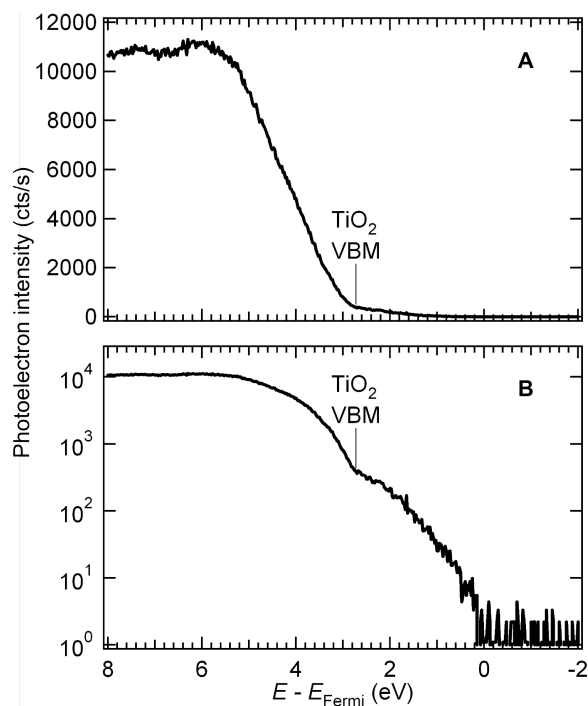


Fig. S1 UPS spectrum of the TiO<sub>2</sub> (110) surface cleaned according to the procedure described and receiving no further surface treatment *in vacuo*. The photoemission intensity in the vicinity of the valence band maximum (VBM) is presented on both linear (**A**) and logarithmic (**B**) scales. The position of the VBM is determined by the kink in the log scale representation marking the transition from occupied “true” valence band states to the continuum of defect-induced surface states extending to the Fermi level. The VBM is  $2.7 \pm 0.1$  eV below the Fermi level, placing the conduction band minimum (CBM) 0.3 eV above  $E_{\text{Fermi}}$ .

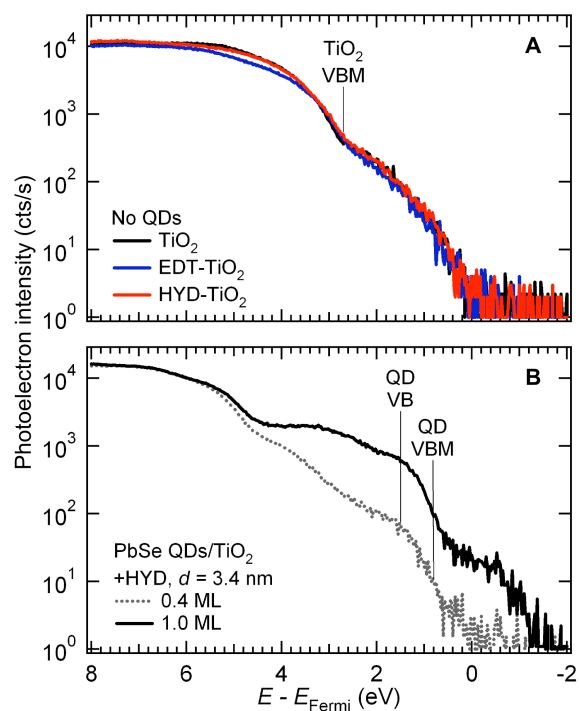


Fig. S2 (A) UPS spectra of the bare  $\text{TiO}_2$  (110) surface treated for 10 min with HYD or 30 s with EDT but without any PbSe nanocrystals. The UPS spectrum is unchanged by chemical treatment over this energy range. (B) UPS spectra of the  $\text{TiO}_2$  (110) surface covered with 0.4 monolayers (ML) or 1.0 ML of 3.4 nm PbSe nanocrystals treated with HYD. PbSe valence band (VB) features are evident within the band gap of  $\text{TiO}_2$ . The highest occupied nanocrystal energy level, or valence band maximum (VBM), is determined by the inflection point in the photoemission spectrum.

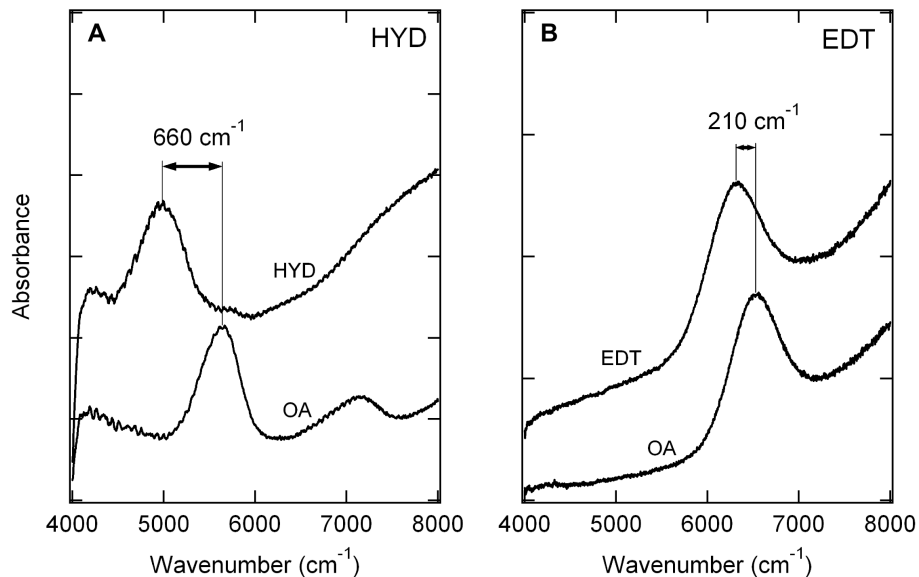


Fig. S3 Dependence of the first exciton peak position of PbSe nanocrystals in a 1-2 ML film on chemical treatment of the nanocrystal surface. **(A)** 5.8 nm diameter PbSe nanocrystals capped with the native oleic acid (OA) ligands and after exposure to 1.0 M hydrazine (HYD) in acetonitrile for 10 min. The first exciton peak shifts  $660\text{ cm}^{-1}$  (82 meV) toward the red following HYD treatment. **(B)** 5.0 nm diameter PbSe nanocrystals capped with the native OA ligands and after exposure to 0.1 M 1,2-ethanedithiol (EDT) in acetonitrile for 30 s. The first exciton peak shifts only  $210\text{ cm}^{-1}$  (26 meV) toward the red following EDT treatment. Note the cutoff at the low frequency end was due to the InGaAs detector.

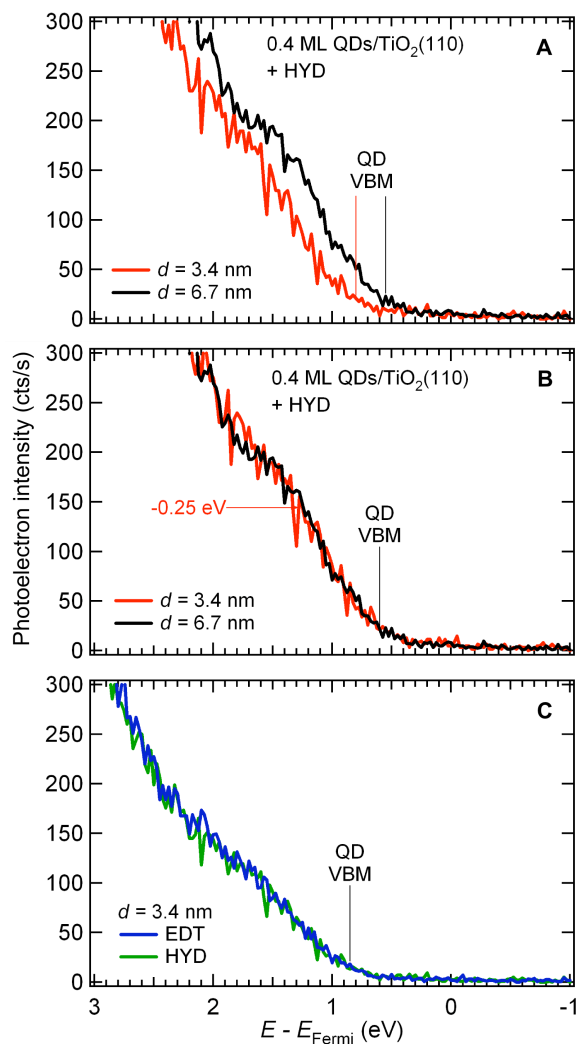


Fig. S4 Dependence of interfacial energy alignment on nanocrystal size and chemical treatment. (A) UPS spectra of HYD-treated PbSe nanocrystal films for two different size nanocrystals,  $d = 3.4$  nm and  $d = 6.7$  nm. The locations of the valence band maximum (VBM – determined from log scale inflection points) are indicated by color-coded vertical lines. The intensity of the  $d = 3.4$  nm data has been scaled to match the intensity at  $d = 6.7$  nm. (B) The same data shown in (A), but the  $d = 3.4$  nm trace has been shifted horizontally toward lower binding energy by 0.25 eV to demonstrate the energy alignment difference between the two sizes. (C) UPS spectra of 0.4 ML  $d = 3.4$  nm PbSe nanocrystals after HYD or EDT treatment. The energetic alignment is the same for both treatments. Similar results are obtained at  $d = 6.7$  nm.

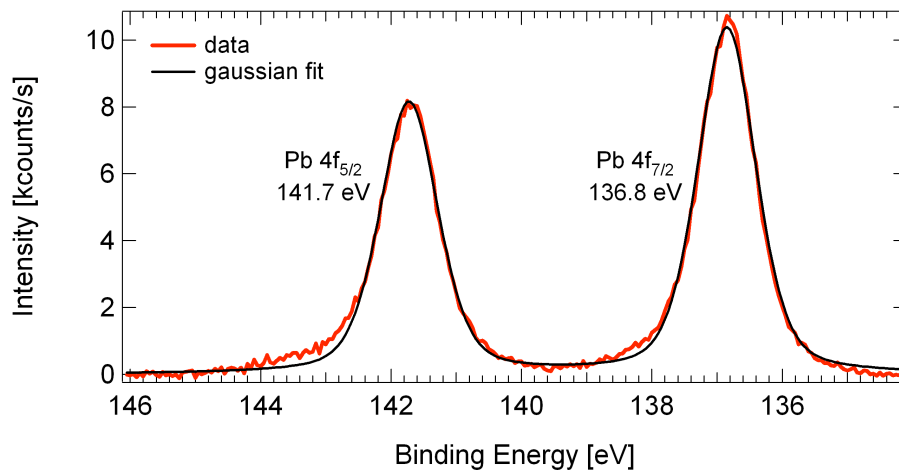


Fig. S5 XPS spectrum in the vicinity of Pb 4f core level photoemission. The sample is 1 ML PbSe nanocrystals on TiO<sub>2</sub> (110) treated with HYD. This spectrum was collected after typical daily TR-SHG measurements. Following laser experiments, the sample was transferred to a sealed vessel inside the glovebox for air-free transfer to the XPS vacuum chamber. The XPS spectrum shows two gaussian peaks without significant asymmetry toward higher binding energies, indicating that the PbSe surface is free from oxidation. A linear background has been subtracted.

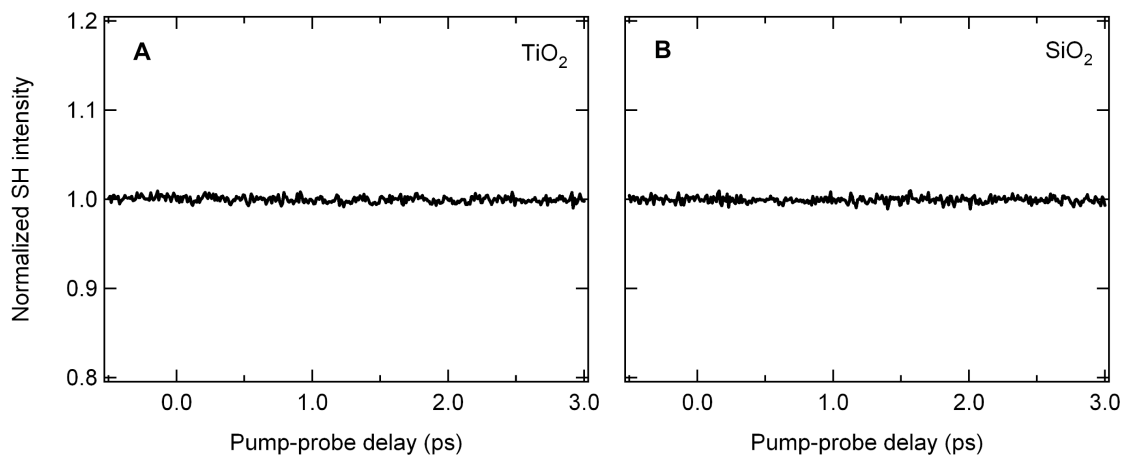


Fig. S6 TR-SH response at 80 K of (A) the bare TiO<sub>2</sub> (110) surface and (B) the bare SiO<sub>2</sub> (amorphous fused silica) surface. The TR-SH response is featureless for HYD- or EDT-treated substrates (without nanocrystals) as well.

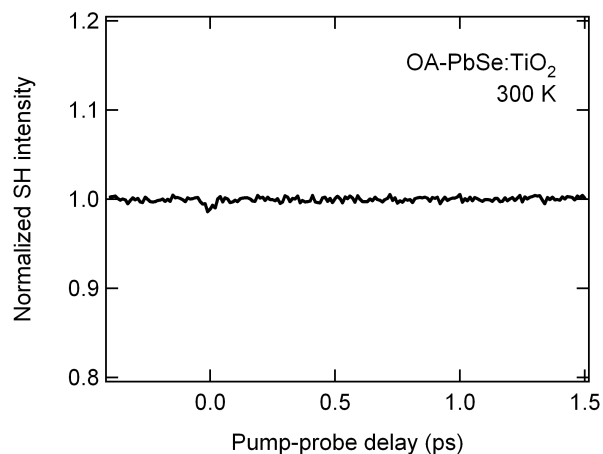


Fig. S7 TR-SH response at 300K of oleic acid (OA)-capped PbSe nanocrystals ( $d = 6.1$  nm) on TiO<sub>2</sub>. The 18-carbon aliphatic straight-chain ligand insulates the PbSe core from strong electronic interaction with the substrate, preventing hot electron transfer. The small dip at  $t = 0$  is a coherent artifact arising from temporal overlap of the pump and probe beams with parallel polarization. TR-SH waveforms are featureless (within our signal-to-noise capabilities) for all OA-capped PbSe nanocrystals, regardless of nanocrystal size, temperature, or substrate material.

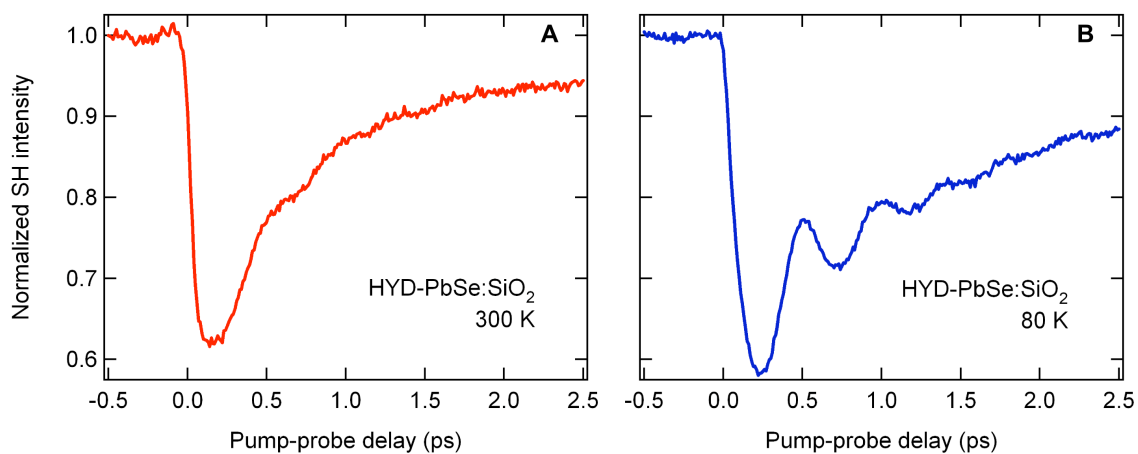


Fig. S8 TR-SH response of hydrazine (HYD)-treated PbSe nanocrystals ( $d = 6.7$  nm) on SiO<sub>2</sub> at (A) 300 K and (B) 80 K. The SH signal recovers faster at 300 K ( $\sim 0.5$  ps time constant) than at 80 K ( $\sim 3$  ps time constant). Coherent phonon oscillations are more evident at lower temperatures due to slower dephasing.

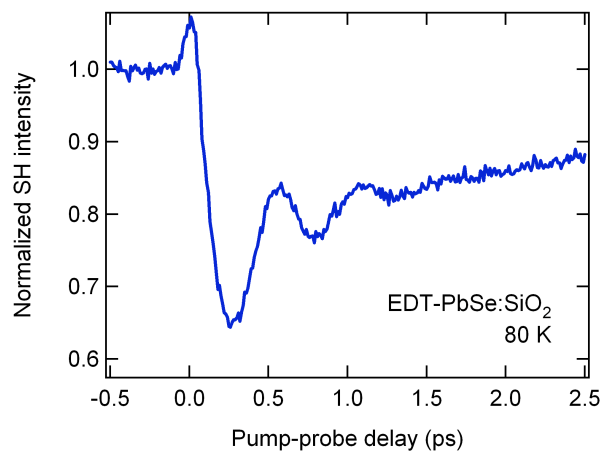


Fig. S9 TR-SH response of PbSe nanocrystals ( $d = 6.7$  nm) on SiO<sub>2</sub> treated with 1,2-ethanedithiol (EDT) at 80 K. The response is similar to that of HYD-treated nanocrystals on SiO<sub>2</sub> (Fig. S8).

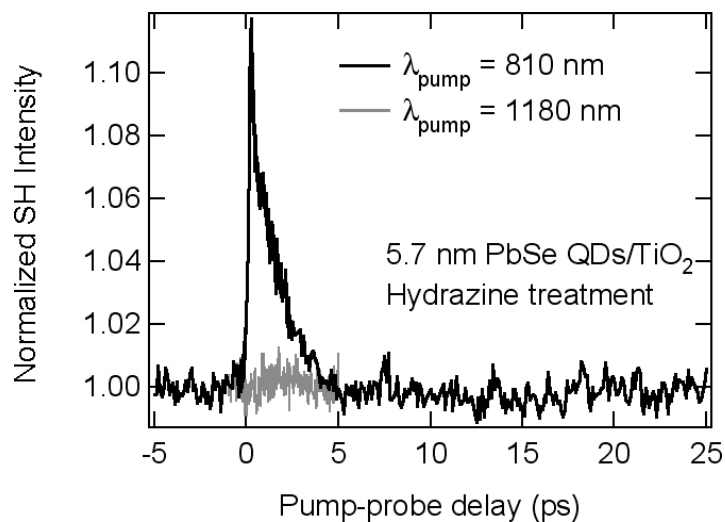


Fig. S10 TR-SH response of PbSe nanocrystals ( $d = 5.7$  nm) on  $\text{TiO}_2$  (treated with hydrazine) at 80 K for two different pump laser wavelengths:  $\lambda_{\text{pump}} = 810$  nm (black) and  $\lambda_{\text{pump}} = 1180$  nm (grey). The laser power at each wavelength was chosen to maintain an average excitation of 1.0 electron-hole pairs per nanocrystal.

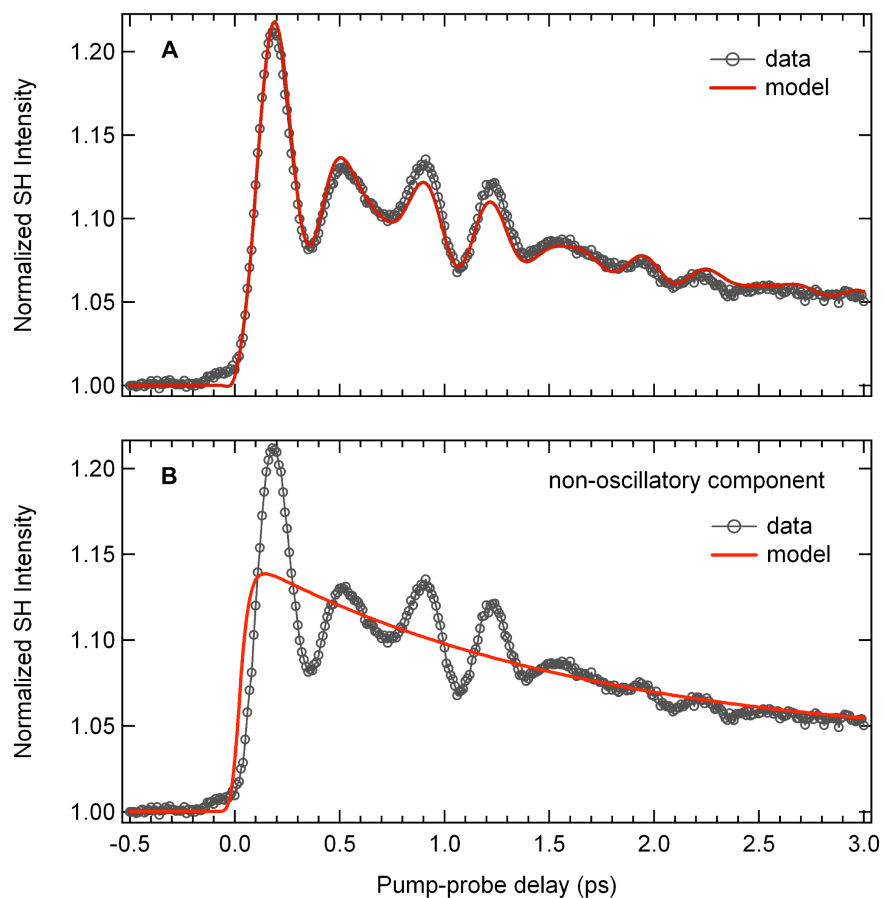


Fig. S11 Results of TR-SHG curve-fitting to the data shown in Fig. 4A, based on a phenomenological model for the EFISH response. We extract an electron transfer time constant of  $31 \pm 5$  fs. Three sine components are included in the fitting function, with best-fit frequencies  $66.8 \text{ cm}^{-1}$ ,  $95.3 \text{ cm}^{-1}$ , and  $131.0 \text{ cm}^{-1}$ ; phase  $3\pi/2$ ,  $3\pi/2$ , and  $\pi$ ; and dephasing times 520 fs, 1100 fs, and 950 fs, respectively. **(A)** The entire best-fit TR-SH waveform. **(B)** The non-oscillatory part of the TR-SH signal, revealing the underlying electron transfer dynamics.

## 6. Supplementary Tables

Table S1 Summary of interfacial energy levels (eV) referenced to the Fermi level ( $E_F = 0.0$  eV) as determined by UPS and FT-NIR. These are the values plotted in Fig. 1C. All values have an estimated uncertainty of  $\pm 0.1$  eV.

	Substrate Bands		PbSe nanocrystals + hydrazine				PbSe nanocrystals + EDT			
			$d = 6.7$ nm		$d = 3.4$ nm		$d = 6.7$ nm		$d = 3.4$ nm	
	VBM	CBM	HOMO	LUMO	HOMO	LUMO	HOMO	LUMO	HOMO	LUMO
TiO <sub>2</sub>	-2.7	0.3	-0.55	0.00	-0.80	0.17	-0.55	0.05	-0.80	0.30

## 7. References

- S1. J. E. Murphy, M. C. Beard, A. J. Nozik, *J. Phys. Chem. B* **110**, 25455 (2006).  
S2. J. M. Luther *et al.*, *ACS Nano* **2**, 271 (2008).  
S3. Q. Q. Dai *et al.*, *ACS Nano* **3**, 1518 (2009).  
S4. I. Moreels *et al.*, *Chem. Mater.* **19**, 6101 (2007).  
S5. Y. F. Lu, D. J. Choi, J. Nelson, O. B. Yang, B. A. Parkinson, *J. Electrochem. Soc.* **153**, E131 (2006).  
S6. M. Law *et al.*, *J. Am. Chem. Soc.* **130**, 5974 (2008).  
S7. K. J. Williams *et al.*, *ACS Nano* **3**, 1532 (2009).  
S8. B. V. Crist, *Handbook of monochromatic XPS spectra* (Wiley, New York, 2000).  
S9. B. R. Hyun *et al.*, *ACS Nano* **2**, 2206 (2008).  
S10. X. M. Jiang *et al.*, *J. Mater. Res.* **22**, 2204 (2007).  
S11. J. Pascual, J. Camassel, H. Mathieu, *Phys. Rev. B* **18**, 5606 (1978).  
S12. F. W. Wise, *Acc. Chem. Res.* **33**, 773 (2000).  
S13. C. Gautier, M. Cambon-Muller, M. Averous, *Appl. Surf. Sci.* **141**, 157 (1999).  
S14. J. C. Johnson *et al.*, *Nano Lett.* **4**, 197 (2004).  
S15. R. D. Schaller *et al.*, *Phys. Rev. Lett.* **95**, 196401 (2005).  
S16. N. Bloembergen, C. H. Lee, *Phys. Rev. Lett.* **19**, 835 (1967).  
S17. B. Dick, A. Gierulski, G. Marowsky, G. A. Reider, *Appl. Phys. B* **38**, 107 (1985).  
S18. M. Ben-Lulu *et al.*, *Nano Lett.* **8**, 1207 (2008)].  
S19. C. H. Lee, R. K. Chang, N. Bloembergen, *Phys. Rev. Lett.* **18**, 167 (1967).  
S20. T. F. Heinz, in *Nonlinear Surface Electromagnetic Phenomena*, H. Ponath, G. I. Stegeman, Eds. (Elsevier, Amsterdam, 1991), pp. 353-416.  
S21. O. A. Aktsipetrov *et al.*, *Phys. Rev. B* **60**, 8924 (1999).  
S22. P. Guyot-Sionnest, W. Chen, Y. R. Shen, *Phys. Rev. B* **33**, 8254 (1986).  
S23. M. Omote *et al.*, *J. Phys. Cond. Matter* **17**, S175 (2005).  
S24. A. Nahata, T. F. Heinz, *Opt. Lett.* **23**, 67 (1998).  
S25. Y. Matsumoto, K. Watanabe, *Chem. Rev.* **106**, 4234 (2006).  
S26. V. V. Meriakri, E. F. Ushatkin, *Instrum. Exp. Tech.* **16**, 143 (1973).  
S27. S. E. Kohn *et al.*, *Phys. Rev. B* **8**, 1477 (1973).  
S28. K. F. Brennan, *The Physics of Semiconductors* (Cambridge University Press, 1999).  
S29. J. F. Baumard, F. Gervais, *Phys. Rev. B* **15**, 2316 (1977).  
S30. K. M. Glassford, J. R. Chelikowsky, *Phys. Rev. B* **46**, 1284 (1992).